A new insight into the vertical differences in NO_2 heterogeneous reaction to produce HONO over inland and marginal seas

Chengzhi Xing[1], Shiqi Xu[7], Yuhang Song[2], Cheng Liu[2,1,3,4,*], Yuhan Liu[6], Keding Lu[5,*], Wei Tan[1], Chengxin Zhang[2], Qihou Hu[1], Shanshan Wang[9], Hongyu Wu[8], and Hua Lin[8]

[1] Key Lab of Environmental Optics & Technology, Anhui Institute of Optics and Fine Mechanics, Hefei Institutes of Physical Science, Chinese Academy of Sciences, Hefei 230031, China

[2] Department of Precision Machinery and Precision Instrumentation, University of Science and Technology of China, Hefei, 230026, China

[3] Center for Excellence in Regional Atmospheric Environment, Institute of Urban Environment, Chinese Academy of Sciences, Xiamen, 361021, China

[4] Key Laboratory of Precision Scientific Instrumentation of Anhui Higher Education Institutes, University of Science and Technology of China, Hefei, 230026, China

[5] State Key Joint Laboratory of Environment Simulation and Pollution Control, College of Environmental Sciences and Engineering, Peking University, Beijing 100871, China

[6] Department of unclear safety, Chia Institute of Atomic Energy, Beijing, 102413, China

[7] School of Earth and Space Sciences, University of Science and Technology of China, Hefei, 230026, China.

[8] School of Environmental Science and Optoelectronic Technology, University of Science and Technology of China, Hefei, 230026, China

[9] Shanghai Key Laboratory of Atmospheric Particle Pollution and Prevention (LAP[3]), Department of Environmental Science and Engineering, Fudan University, Shanghai, 200433, China

*Corresponding authors: Cheng Liu (chliu81@ustc.edu.cn); Keding Lu (k.lu@pku.edu.cn)

1   **ABSTRACT**
2   Ship based multi-axis differential optical absorption spectroscopy (MAX-DOAS) measurements were conducted
3   along the marginal seas of China from 19 April to 16 May 2018 to measure the vertical profiles of aerosol, nitrogen
4   dioxide (NO_2), and nitrous acid (HONO). Along the cruise route, we found five hot spots with enhanced
5   tropospheric NO_2 VCDs in Yangtze River Delta, Taiwan straits, Guangzhou-Hong Kong-Macao Greater Bay areas,
6   Zhanjiang Port, and Qingdao port. Enhanced HONO concentrations could usually be observed under high-level
7   aerosol and NO_2 conditions, whereas the reverse was not always the case. To understand the impacts of relative
8   humidity (RH), temperature, and aerosol on the heterogeneous reaction of NO_2 to form HONO in different scenes, the
9   Chinese Academy of Meteorological Sciences (CAMS) and Southern University of Science and Technology (SUST)
10   MAX-DOAS stations were selected as the inland and coastal cases, respectively. The RH turning points in CAMS and
11   SUST cases were both ~65% (60–70%), whereas two turning peaks (~60% and ~85%) of RH were found in the sea
12   cases. As temperature increased, the HONO/NO_2 ratio decreased with peak values appearing at ~12.5℃ in CAMS,
13   whereas the HONO/NO_2 gradually increased and reached peak values at ~31.5℃ in SUST. In the sea case, when the
14   temperature exceeded 18.0℃, the HONO/NO_2 ratio rose with increasing temperature and achieved its peak at ~25.0℃.
15   This indicated that high temperature can contribute to the secondary formation of HONO in the sea atmosphere. In the
16   inland case, the correlation analysis between HONO and aerosol in the near-surface layer showed that the ground
17   surface is more crucial to the formation of HONO via the heterogeneous reaction of NO_2; however, in the coastal and
18   sea cases, the aerosol surface contributed more. Furthermore, we discovered that the conversion rate of NO_2 to HONO
19   through heterogeneous reaction in the sea case is larger than that in the inland case in higher atmospheric layers (>
20   600 m). Three typical events were selected to demonstrate three potential contributing factors of HONO production
21   under marine conditions (i.e., transport, NO_2 heterogeneous reaction, and unknown HONO source). This study
22   elucidates the sea-land and vertical differences in the forming mechanism of HONO via the NO_2 heterogeneous
23   reaction and provides deep insights into tropospheric HONO distribution, transforming process, and environmental
24   effects.
25

26   **1 Introduction**

27   Nitrous acid (HONO) is an important part of the atmospheric nitrogen cycle and plays a significant role in
28   atmospheric oxidation capacity (Alicke et al., 2003; Kleffmann et al., 2005). Photolysis of HONO in near ultraviolet
29   bands (Eq. 1) is a substantial source of hydroxyl radicals (OH radicals), which are one of the most important oxidants
30   in the tropospheric atmosphere. Earlier studies reported that the contribution of HONO photolysis to OH radicals can

31 reach 40–60%, while exceeding 80% in the early morning (Michoud et al., 2012; Ryan et al., 2018; Xue et al., 2020).
32 OH radicals can oxidize and destroy most atmospheric pollutants, such as CO, NO_x (NO+NO₂), SO₂, and volatile
33 organic compounds (VOCs), thereby further promoting the formation of secondary pollutants (e.g., ozone (O₃),
34 peroxyacetyl nitrate (PAN), and secondary aerosols) and leading to serious haze pollution events (Huang et al., 2014).
35 Additionally, as a nitrosating agent, HONO can produce carcinogenic nitrite amines that pose a threat to human health
36 (Zhang et al., 2015). Therefore, a full understanding of the source and formation mechanism of HONO is
37 scientifically significant for the study of tropospheric oxidation and the control of secondary pollution.

38 Currently, the known sources of HONO mainly include direct emissions from vehicles, ships, biomass burning and
39 soil, the homogeneous reaction of NO and OH radicals (Eq. 2), the nighttime and daytime heterogeneous reaction of
40 NO₂ (Eq. 3) on aerosols, vegetation, ground and other types of surfaces, and the photolysis of nitrate particles (Eq. 4)
41 (Alicke et al., 2003; Stemmer et al., 2006; Indarto et al., 2012; Wang et al., 2015; Salgado and Rossi, 2002; Zhou et
42 al., 2011). Sources of HONO exist that are poorly understood (Fu et al., 2019). The heterogeneous reaction of NO₂ as
43 a source of HONO has received continuous attention in recent years. It was found that the heterogeneous reaction of
44 NO₂ is one of the most important sources of HONO in a variety of scenes such as inland, coastal cities, and offshore
45 seas. Liu et al. (2021) reported the contribution of heterogeneous reaction of NO₂ on aerosol surface to HONO is
46 19.2% in summer, and this contribution on aerosol and ground surfaces to HONO can reach 54.6% in winter in
47 Beijing. Yang et al. (2021) and Zha et al. (2014) found that the generation rate of HONO through the heterogeneous
48 reaction of NO₂ under sea-wind conditions could elevate 3–4 times than that under land-wind conditions in the
49 northern coastal city of Qingdao and the southern coastal city of Hong Kong, respectively. Cui et al. (2019) illustrated
50 that the heterogeneous reaction of NO₂ on aerosol and sea surfaces is an important source of HONO in East China Sea
51 in summer. The process of HONO formed from the heterogeneous reaction of NO₂ is affected by various atmospheric
52 parameters. The relative humidity (RH), temperature, solar radiation intensity (SRI), and aerosol concentration and its
53 relative surface area are the particularly important parameters. Earlier works always used the linear regression
54 relationship between HONO/NO₂ and the above parameters to characterize the influence of these parameters on the
55 formation of HONO through the heterogeneous reaction of NO₂. Although this kind of simple linear regression
56 method may lead to artificial correlations and misleading conclusions, considering the vertical evolution of
57 atmospheric parameters. Wen et al. (2019) found that the increased temperature could promote the heterogeneous
58 reaction of NO₂ to form HONO in sea conditions. The generation rate of HONO could increase rapidly, when the
59 temperature was greater than 20 ℃. Gil et al. (2019) found that the HONO formed from the heterogeneous reaction of
60 NO₂ will increase along with the increase of RH when RH was less than 80% in a case of land park using deep
61 learning forced by measurement results. Fu et al. (2019) reported that RH and SRI were the main parameters driving
62 the heterogeneous reaction of NO₂ to form HONO in Pearl River Delta, and it contributes to 72% of the total source
63 of HONO. Cui et al. (2019) found that the potential of heterogeneous reaction of NO₂ to form HONO will increase
64 with the increase of particle concentration and the specific surface area of single particle in coastal cities.

65 $$HONO + hv \rightarrow NO + \cdot OH \, (\lambda < 400nm) \tag{1}$$

66 $$\cdot OH + NO + M \rightarrow HONO + M \tag{2}$$

67 $$2NO_2 + H_2O \rightarrow HONO + HNO_3 \tag{3}$$

68 $$HNO_3 / NO_3^- + hv \rightarrow HONO / NO_2^- + O \cdot (\lambda \sim 300nm) \tag{4}$$

69 However, earlier researches generally focused on the near-surface layer of a single scene, and attentions to the
70 influence mechanism of the heterogeneous reaction of NO₂ to form HONO in vertical direction and in different sea
71 and land scenes are insufficient, which limits the comprehensive assessment to understand the sea-land differences
72 and impact mechanism of HONO formed from the heterogeneous reaction of NO₂. NO₂ could be transported from
73 inland and coastal cities to offshore seas (Tan et al., 2018). This part of NO₂ can promote the HONO formation
74 through heterogeneous reaction on the high-level aerosol and sea surfaces in the atmosphere of sea (Zhang et al.,
75 2020). The formed HONO is likely to be carried to land cities at night by sea breeze, which will affect the
76 atmospheric oxidation and air quality, and even endanger human health. Additionally, the vertical distributions and
77 values of atmospheric meteorology and aerosol parameters are significantly different in land and sea scenes, which
78 provide different conditions for the heterogeneous reaction of NO₂ to form HONO in different height layers.
79 Furthermore, aerosols and NO₂ have complex evolution and transmission characteristics in the vertical direction. The
80 vertical upward transport of aerosol and NO₂ can promote the HONO formation through heterogeneous reaction at
81 high altitude, and the vertical downward transport of HONO will impact the atmospheric environment near the ground.
82 The vertical observations in land-sea scenes are also helpful to distinguish the contribution of the heterogeneous
83 reaction of NO₂ on the aerosol and ground/sea surfaces (Zhang et al., 2020).

84 Currently, a variety of HONO measurement techniques have been developed, which in principle can be roughly
85 divided into wet chemical, spectroscopy, and mass spectrometry methods (Cheng et al., 2013; Bernard et al., 2016;
86 Gil et al., 2019; Guo et al., 2020; Jordan et al., 2020). However, these technical methods can only measure the HONO

87 information near the surface layer. Taking tower and aircraft as platforms, these techniques were performed to
88 measure HONO vertical profiles, and it was found that the peak values of HONO usually appeared under 200 m at
89 urban and suburban areas (Kleffmann et al., 2003; Stemmler et al., 2006; Zhang et al., 2009; Wong et al., 2012; Meng
90 et al., 2020; Zhang et al., 2020). These studies also revealed that the heterogeneous reaction of NO_2 on multiple
91 surfaces (ground and aerosol etc.) was an important source of HONO under planetary boundary layer (PBL),
92 especially in haze days. Furthermore, they also reported that the $HONO/NO_2$ ratios usually decreased with the
93 increase of height under 200 m at inland and coastal areas. However, the cost of above techniques used to measure
94 HONO vertical profiles was too high, and the real-time and continuous measurement cannot be realized. Multi-axis
95 differential optical absorption spectroscopy (MAX-DOAS), as a ground-based ultra-hyperspectral remote sensing
96 technology, was widely used for vertical observation of atmospheric pollutants in the past two decades. In the past
97 five years, several researchers carried out campaigns based on MAX-DOAS to measure the vertical profile of HONO
98 in inland and coastal areas, and revealed their vertical characteristics, sources, and the contribution to atmospheric
99 oxidation at different height layers (Garcia-Nieto et al., 2018; Ryan et al., 2018; Wang et al., 2020; Xing et al., 2021;
100 Xu et al., 2021; He et al., 2023). Few studies were conducted on the sources of HONO at different height layers in sea
101 conditions. In this study, MAX-DOAS is used for the first time to study the spatiotemporal distribution and the
102 sources of HONO along the Chinese coastline, and to learn the differences of the HONO formed from the
103 heterogeneous reaction of NO_2 in different height layers and land-sea scenes.

2 Methods and methodologies

2.1 Measurement cruise

106 The ship-based atmospheric observation campaign along the marginal seas of China was conducted from 19 April to
107 16 May 2018. The latitude and longitude ranges of the entire campaign covered 21.12°N–35.89°N and
108 110.67°E–122.16°E. The detailed voyage records of the observation ship are shown in Table 1. An integrated and
109 fully automated MAX-DOAS instrument was installed aboard the stern deck of the ship (Figure S1(a)). To ensure that
110 the instrument is always kept in a horizontal position, a photoelectric gyro was used. The angle between the
111 observation and heading directions of the ship was always maintained at 135° during the whole campaign. The
112 telescope unit of the instrument pointed towards sea during cruise NO.3 and NO.6. The telescope unit pointed towards
113 inland during cruise NO.1, NO.4, and NO.5. During cruise NO.2, the observation telescope always pointed to
114 Chongming island. The measurement ship only sailed in daytime from 19 April to 02 May, and continuously sailed in
115 all the daytime and nighttime from 3 May to 16 May 2018. The ship docked in Daishan port on 9–10 May and no
116 observations were conducted during these two days.

117 The aim of this campaign was to learn the vertical differences of NO_2 heterogeneous reaction to produce HONO in
118 marginal seas of China and compare the influence mechanism of that in inland cities. To fully understand the
119 differences of the impacts of RH, temperature, and aerosol on the HONO secondary formation in land and sea
120 conditions, the Chinese Academy of Meteorological Sciences (CAMS) and Southern University of Science and
121 Technology (SUST) MAX-DOAS stations were selected as inland and coastal areas for analysis, respectively. CAMS
122 is located in the urban of Beijing (116.32°E, 39.94°N), and SUST is located in Shenzhen (114.00°E, 22.60°N) (Figure
123 S2). This study will provide scientific guidance for understanding regional oxidation capacity and controlling the
124 secondary air pollution.

2.2 MAX-DOAS measurements

2.2.1 Instrument setup

127 The compact instrument consists of an ultraviolet spectrometer (AvaSpec-ULS2048L-USB2, 300–460 nm spectral
128 range, 0.6 nm spectral resolution) at a 20℃ fixed temperature with a deviation of < 0.01℃, a one-dimensional CCD
129 detector (Sony ILX511, 2048 individual pixels) and a telescope unit driven by a stepper motor to collect scattered
130 sunlight from different elevation angles. The accuracy of elevation angle is < 0.1° and the telescope field of view
131 (open angle) is < 0.3°. A full scanning sequence consists of 11 elevation angles (1°, 2°, 3°, 4°, 5°, 6°, 8°, 10°, 15°, 30°,
132 and 90°). The integration time of one individual spectrum was set to 30 s, and each scanning sequence took about 5.5
133 min. Besides, the controlling electronic devices and connecting fiber are mounted inside. The instrument is equipped
134 with a high-precision Global Position System (GPS) to record the real-time coordinated positions of the cruise ship.
135 The detailed description of the setup of MAX-DOAS in CAMS and SUST can be found in Liu et al. (2021).

2.2.2 Data processing and filtering

137 The MAX-DOAS measurements could be influenced by the exhaust from the measurement ship. Therefore, the data
138 contaminated by the exhaust were filtered out. As shown in Figure S1(b), the direction and speed of the plume
139 exhausted from the ship depends on the ship and the true wind speeds/directions. Individual measurements taken
140 under unfavorable plume directions (plume directions between 45 and 135° with respect to the heading of the ship)
141 were discarded. To avoid the strong influence of the stratospheric absorption, the spectra measured with solar zenith
142 angle (SZA) lager than 75 ° were filtered out. Under these two filtering criteria, 4.9 and 8.3% of all data were rejected
143 before DOAS analysis (Xing et al., 2017, 2019, 2020).

2.2.3 DOAS analysis

The MAX-DOAS measured spectra were analyzed using the software QDOAS which is developed by BIRA-IASB (http://uv-vis aeronomie.be/software/QDOAS/). The DOAS fit results are the differential slant column densities (DSCDs), i.e. the difference of the slant column density (SCD) between the off-zenith and the corresponding zenith reference spectra. Details of the DOAS fit settings are listed in Table1. A typical DOAS retrieval example for the oxygen dimer (O_4), nitrogen dioxide (NO_2), and nitrous acid (HONO) are shown in Figure 1. The stratospheric contribution was approximately eliminated by taking the zenith spectra of each scan as reference in the DOAS analysis. Before profile retrieval, DOAS fit results of O_4, NO_2, and HONO with root mean square (RMS) of residuals larger than 3×10^{-3} were filtered. Furthermore, the SCD data under the color index (CI) being < 10% of the thresholds obtained through fitting a fifth-order polynomial to CI data which is a function of time was filtered out to ensure a high signal-to-noise ratio (SNR) of the spectra. This filtering criteria remove 2.1, 3.9, and 5.3% for O_4, NO_2, and HONO, respectively.

2.3 Vertical profile retrieval

Aerosol and trace gases (i.e., NO_2 and HONO) vertical profiles are retrieved from MAX-DOAS measurements using the algorithm reported by Liu et al. (2021). The inversion algorithm is developed based on the Optical Estimation Method (OEM) (Rodgers, 2000), which employs the radiative transfer model VLIDORT as the forward model. The detailed retrieval procedure is displayed in Appendix I and Figure S3.

In this study, an exponential decreasing a priori with a scale height of 1.0 km was used as the initial profile for both the aerosol and trace gases retrieval (Figure S4). The surface concentrations of aerosol, NO_2, and HONO were set to 0.2 km^{-1}, 3.0 ppb, and 1.0 ppb, respectively. We assume a fix set of aerosol optical properties with asymmetry parameter of 0.69, a single scattering albedo of 0.90, and ground albedo of 0.05. Furthermore, the uncertainty of the aerosol and trace gases a priori profile was set to 100% and the correlation length was set to 0.5 km. The averaging kernels indicated that the sensitivity of the profile retrieval tended to decrease with increasing altitude, and was especially sensitive to the layers within 0–1.5 km (Figure S5). The sum of the diagonal elements in the averaging kernel matrix is the degrees of freedom (DOF), which denotes the number of independent pieces of information contained in the measurements.

2.4 Error analysis

For profile retrieval, the error sources can be divided into four different types: smoothing error, measurement noise error, forward model error, and model parameter error (Rodgers, 2004). However, in terms of this classification, some errors are difficult to be calculated or estimated. For example, forward model error, which is caused by an imperfect representation of the physics of the system, is hard to be quantified due to the difficulty of acquiring an improved forward model. Given calculation convenience and contributing ratios of different errors in total error budget, we mainly took into account error sources based on the following classification, which were smoothing and noise errors, algorithm error, cross section error, and uncertainty related to the aerosol retrieval (only for trace gas). Here, we estimated the contribution of different error sources to the trace gas vertical column densities (VCDs) and AOD, and near-surface (0–200 m) trace gas concentrations and aerosol extinction coefficients (AECs), respectively. The detailed demonstrations and estimation methods are displayed below, and the final results are summarized in Table 3.

a. Smoothing errors arise from the limited vertical resolution of profile retrieval. Measurement noise errors denote the noise in the spectra (i.e., the fitting error of DOAS fits). They can be quantified by averaging the error of retrieved profiles, as the error of the retrieved state vector equals the sum of these two independent errors. We calculated the sum of smoothing and noise errors on near-surface concentrations and column densities, which were 14 and 5 % for aerosols, 16 and 17 % for NO_2, and 20 and 22 % for HONO, respectively in the sea scene. The corresponding values were 13 and 5 % for aerosols, 14 and 16 % for NO_2, and 18 and 20 % for HONO, respectively at SUST and 13 and 5 % for aerosols, 15 and 17 % for NO_2, and 19 and 21 % for HONO at CAMS.

b. Algorithm error is the discrepancy between the measured and modelled DSCDs. This error contains forward model error from an imperfect approximation of forward function (e.g., spatial inhomogeneities of absorbers and aerosols), forward model parameter error from selection of parameters, and error not related to the forward function parameters, such as detector noise (Rodgers, 2004). Algorithm error is a function of the viewing angle, and it is difficult to assign this error to each altitude of profile. Usually, the algorithm errors on the near-surface values and column densities are estimated by calculating the average relative differences between the measured and modeled DSCDs at the minimum and maximum elevation angle (except 90 °), respectively (Wagner et al., 2004). Considering its trivial role in the total error budget, we estimated these errors on the near-surface values and the column densities at 4 and 8 % for aerosols, 3 and 11 % for NO_2, and 20 and 20 % for HONO, according to Wang et al. (2017) and Wang et al. (2020).

c. Cross section error is the error arising from an uncertainty in the cross section. According to Thalman and Volkamer, (2013), Vandaele et al. (1998), and Stutz et al. (2000), we adopted 4, 3, and 5 % for O_4 (aerosols), NO_2, and HONO, respectively.

d. The trace gas profile retrieval error represents the one, which is sourced from aerosol extinction profile retrieval and propagated to retrieved trace gas profile. This error could be roughly estimated based on a linear propagation of the total error budgets of the aerosol retrievals. The errors of trace gases were roughly estimated at 15% for

204 VCDs and 10% for near-surface concentrations for the two trace gases in the sea scene. The corresponding values
205 were 14 and 10 % for near-surface concentrations and VCDs, respectively at SUST, and 14 and 10 % at CAMS.
206 The total uncertainty was calculated by adding all the error terms in the Gaussian error propagation, and the final
207 results were listed in the bottom row of Table 3. We found that the sum of smoothing and noise errors played a
208 dominant role in the total uncertainty.

2.5 Ancillary data

210 Meteorological data (including temperature, pressure, relative humidity, visibility, solar radiation intensity, wind
211 speed, and wind direction) with a temporal resolution of 1 min was measured in the weather station installed on the
212 ship. NO was measured using NO analyzer (Thermo Scientific model 42i) with a 1 min resolution. The speed of the
213 ship was calculated referring to the GPS data.
214 The temperature and relative humidity of two ground-based stations (i.e., CAMS and SUST) were collected from
215 Weather Underground website, temporal resolution of which is around 3 hours.
216 The backward trajectory was calculated using HYSPLIT (Hybrid Single-Particle Lagrangian Integrated Trajectory)
217 developed by the National Oceanic and Atmospheric Administration Air Resource Laboratory (NOAA-ARL). The
218 meteorological data with a $1^o \times 1^o$ spatial resolution and 24 layers were collected from the Global Data Assimilation
219 System (GDAS).

3 Results and Discussion

3.1 Overview of the MAX-DOAS observation over marginal seas of China

222 A radiative transfer model SCIATRAN was used to convert SCDs of NO_2 and HONO to their tropospheric VCDs.
223 The vertical profiles of aerosol, NO_2, and HONO retrieved from MAX-DOAS, the temperature and pressure vertical
224 profiles simulated using a dynamical-chemical model (WRF-Chem), and the geo-position data collected by GPS were
225 introduced as inputs in SCIATRAN for the NO_2 and HONO air mass factor (AMF) calculation. Missing data are due
226 to power and instrument system failure, interference of ship plume, unfavorable weather condition (i. e., heavy rain),
227 and night sailing. During the cruise of Chongming to Zhanjiang, NO_2 VCDs varied from 1.05×10^{14} to 4.02×10^{16}
228 molec.cm^{-2} with an averaged value of 3.90×10^{15} molec. cm^{-2}. From Zhanjiang to Qingdao, NO_2 VCDs varied from
229 1.08×10^{14} to 2.60×10^{16} molec.cm^{-2} with an averaged value of 4.27×10^{15} molec. cm^{-2}. From Chongming to Zhanjiang,
230 HONO VCDs varied from 1.00×10^{14} to 2.58×10^{15} molec. cm^{-2} with a mean value of 2.39×10^{14} molec. cm^{-2}. From
231 Zhanjiang to Qingdao, HONO VCDs varied from 1.01×10^{14} to 2.61×10^{15} molec. cm^{-2} with a mean value of 2.74×10^{14}
232 molec. cm^{-2}.
233 Figure 2 showed the spatial distribution of NO_2 and HONO VCDs over the marginal seas of China. Five enhanced
234 tropospheric NO_2 VCDs hot spots were observed during the whole campaign, i.e., the coastal areas of Yangtze River
235 Delta, Taiwan straits, Guangzhou-Hong Kong-Macao Greater Bay areas, Zhanjiang Port, and Qingdao port. In the
236 coastal areas of Yangtze River Delta, the hot spots were mainly distributed in the Yangtze River estuary, Hangzhou
237 Bay, Ningbo port, Taizhou port, and Wenzhou port. These areas are mostly important shipping channels or shipping
238 ports, and are great NO_2 emission sources. The averaged NO_2 VCDs in above five areas reached 1.07×10^{16}, 1.30×10^{16},
239 7.27×10^{15}, 5.34×10^{15}, and 3.12×10^{15} molec. cm^{-2}, respectively (Figure S6(a)). HONO exhibited similar spatial
240 distribution characteristics as NO_2, and the averaged HONO VCDs in above five hot-spot areas reached 1.01×10^{15},
241 7.91×10^{14}, 6.02×10^{14}, 5.36×10^{14}, and 5.17×10^{14} molec. cm^{-2}, respectively (Figure S6(b)). It indicates that NO_2 is an
242 important precursor of HONO. Earlier studies reported that HONO can be generated from NO_2 through heterogeneous
243 reaction on the surface of aerosol and sea (Yang et al., 2021). However, there are obvious differences in the
244 concentration distribution of HONO and NO_2 in the southeast coastal area of Jiangsu (from Qidong to Dongtai). In
245 this area, NO_2 showed a higher concentration (1.66×10^{16} molec. cm^{-2}, which is 4 times higher than the mean NO_2
246 VCD), while HONO showed a lower concentration (2.06×10^{14} molec. cm^{-2}, which is ~80% of the mean HONO VCD).
247 It may be the fresh ship emission plume on the route enhancing the NO_2 concentration and HONO has not been fully
248 formed from NO_2 heterogeneous reaction in time, since the observations from ship-based MAX-DOAS are
249 instantaneous.
250 The surface concentration of NO_2 and HONO were extracted from their corresponding vertical profiles. As shown in
251 Figure 3, the total averaged near-surface NO_2 concentrations under sea-oriented and land-oriented measurements were
252 8.46 and 11.31 ppb, respectively. The total averaged near-surface HONO concentrations were 0.23 and 0.27 ppb
253 under sea-oriented and land-oriented measurements. The total averaged near-surface HONO/NO_2 ratios in
254 sea-oriented and land-oriented measurements were 0.027 and 0.024, respectively. Earlier studies reported that vehicle
255 and ship emissions were the main primary HONO sources on land and sea, respectively, and NO_2 heterogeneous
256 reaction on the surfaces of ground, sea, vegetation, and aerosol were the important secondary HONO sources (Liu et
257 al., 2021). Additionally, they found that the surface HONO concentration under the sea case was lower than that under
258 the land case, especially in the morning and evening (Yang et al., 2021). Figure 4 showed the time series of AOD, the
259 surface concentrations of NO_2 and HONO, and the surface HONO/NO_2 during the whole campaign. We found that
260 the time series of AOD and NO_2 were similar. The high AOD and NO_2 usually appeared in busy shipping channels
261 and ports, and the obvious high-value areas were the coast of the Yangtze River Delta, the Taiwan Strait, Xiamen port,
262 Zhanjiang port, and Qingdao port (with mean AOD and NO_2 of 1.28 and 18.90 ppb, respectively). HONO always

263 appeared under high AOD and NO_2 conditions, however, high AOD and NO_2 were not necessarily accompanied with
264 high HONO concentration. This was because the heterogeneous formation of HONO requires suitable meteorological
265 conditions (i.e., RH and temperature) in addition to its precursor (NO_2) and the reaction surface (aerosol) (Liu et al.,
266 2019). The high HONO/NO_2 values were found on 02, 13, and 14 May with an average value of 0.45. Furthermore,
267 we found the high values of HONO/NO_2 always appeared from 11:00 to 14:00 during a whole day.

3.2 Relationship between HONO/NO_2 with RH, Temperature, and aerosol in land and sea

269 Sun et al. (2020) reported that HONO concentrations could increase up to 40–100% over the shipping routes and
270 international ports, and Huang et al. (2017) reported vehicle exhaust could contribute to ~12–49% of the atmospheric
271 HONO budget. Since the direct emissions of the measurement ship were removed before data analysis, the primary
272 source of HONO during the whole campaign was mainly from the direct emissions of cargo ships. By subtracting the
273 average marine background of NO_x and HONO from the ship plume emission values, the impact of background
274 values is reduced and the emission ratio of $\Delta HONO/\Delta NOx$ can be obtained, and this emission ratio can be used for
275 quantifying the primary HONO (Sun et al., 2020; Xu et al., 2015). In this study, we used an averaged 0.46±0.31%
276 emission ratio of $\Delta HONO/\Delta NOx$ referring to Sun et al. (2020) to understand the primary source of HONO on the sea
277 surface during the campaign. The NO was measured using in situ instrument, and sea-surface NO_2 was extracted from
278 the retrieved NO_2 vertical profiles ($NO_x = NO + NO_2$). Additionally, the calculation method of emission ratios of
279 $\Delta HONO/\Delta NOx$ in CAMS and SUST was referred from Xu et al. (2015), Liu et al. (2018), and Xing et al. (2021)
280 (Appendix II). The averaged emission ratios in CAMS and SUST were 0.82±0.34% and 0.79±0.31%, respectively.
281 The direct emissions were deduced in the following study of the secondary formation of HONO. The ratios of
282 HONO/NO_2 in CAMS, SUST, and the ship-based campaign could be found in Figure S7. Furthermore, the main
283 secondary formation pathway of HONO is considered as the heterogeneous reaction of NO_2 on the surface. The linear
284 regression between HONO and NO_2 in land and static sea scenarios is shown in Figure 5. We found the fitting slopes
285 in static sea scenes was ~8–10 times larger than that in land scenes, especially on sea-oriented measurements under
286 static weather condition (slope $\approx$ 0.06). The correlation coefficients (R) in inland and static sea scenarios were all >
287 0.62, except in SUST (R = 0.58), which indicates the formation rate of secondary HONO from NO_2 heterogeneous
288 reaction in static sea scenarios may be faster than that in land scenarios. The corresponding temperature and RH
289 conditions of each spot are displayed in Figure S8, which roughly reveals the impact of RH and temperature on the
290 process of NO_2 forming HONO through heterogeneous reactions.

3.2.1 RH dependence on HONO formation

292 The scatter plots of HONO/NO_2 against RH in different land and sea conditions are illustrated in Figure 6. The
293 highest values can represent varying range of data in each interval and reveal concentration levels of data distribution.
294 To eliminate the influence of other factors, the average of the six highest HONO/NO_2 in each 10% RH interval is
295 calculated to reflect the distribution range of data in each interval (Liu et al., 2019). The dependence of the averaged
296 top-6 HONO/NO_2 on RH reveal an overall variation tendency of HONO/NO_2 against RH. In the inland (CAMS) and
297 coastal (SUST) cases, the RH turning points are both ~65% (60–70%), where increasing trend switches to decreasing
298 tendency. The HONO/NO_2 increases along with RH when RH is less than 65%, and the HONO/NO_2 will decrease
299 when RH is larger than 65%, which implies that it contributes to the HONO formation from the heterogeneous
300 reaction of NO_2 on wet surfaces with the gradual increase of RH until 65%. The decrease of HONO/NO_2 with RH
301 larger than 65% is presumably due to the efficient uptake of HONO on wet surfaces, and the wet surfaces being less
302 accessible or less reactive to NO_2 when RH being larger than 65% (Liu et al., 2019). However, two turning peaks of
303 RH were found in the sea cases. The first RH turning peak occurred in ~60%, which is the similar to that under the
304 inland and coastal cases, and another RH turning peak appeared in ~85% (80–90%). This implies that high RH also
305 could increase the HONO formation in sea cases. Additionally, the HONO/NO_2 decreased sharply when RH was
306 larger than 95%, because the reaction surface will asymptotically approach a water droplet state to limit the formation
307 of HONO with RH larger than 95%.

3.2.2 Temperature dependence on HONO formation

309 The scatter plots of HONO/NO_2 against temperature in different land and sea conditions are shown in Figure 7.
310 Similar to the scatter plots of HONO/NO_2 against RH, we also adopted the averaged top-6 HONO/NO_2 values in each
311 5℃ interval to represent a general variation tendency of HONO/NO_2 against temperature. In the inland condition
312 (CAMS), the HONO/NO_2 decreased along with the increase of temperature, and the highest values of HONO/NO_2
313 appeared at ~12.5℃. However, we found that HONO/NO_2 increased along with the increase in temperature, and the
314 highest values of HONO/NO_2 appeared at ~31.5℃ in coastal condition (SUST), which indicates that the HONO
315 formation from NO_2 heterogeneous reaction will be accelerated under lower and higher temperature in the inland and
316 coastal conditions, respectively. In the sea condition, the HONO/NO_2 increased along with the increase in temperature
317 with a high value under ~25.0℃ when the atmospheric temperature was larger than 18.0℃, and simultaneously, a
318 ~1.9 averaged HONO/NO_2 high value was found under ~15.0℃ (14.0–17.0℃). Furthermore, we found that the
319 appearance of HONO/NO_2 high values under lower temperature (14.0–17.0℃) was usually accompanied by land

6

320 breeze. Wen et al. (2019) also reported that relatively high temperature could contribute to the formation of HONO in
321 the sea condition.

3.2.3 Impact of aerosol on HONO formation

323 To further understand the HONO formation from NO_2 heterogeneous reaction on aerosol surface, several correlation
324 analyses were conducted. As shown in Figure 8, the linear regression plot between HONO and aerosol in land and sea
325 conditions was performed. It was found that the correlation coefficient (R) between HONO and aerosol varied in the
326 order of coastal (0.55) > sea (0.51) > inland (0.14). Additionally, the fitting slopes under coastal and sea conditions
327 (0.07) are about 2.3 times larger than that under inland condition (0.03), which implies that the ground surface maybe
328 more important than aerosol surface during the process of HONO formed from NO_2 heterogeneous reaction in the
329 ground surface layer of the inland. In the coastal and sea conditions, the aerosol and sea are both important in
330 providing heterogeneous reaction surface for NO_2 to form HONO (Cui et al., 2019; Wen et al., 2019; Yang et al.,
331 2021). Additionally, we found the averaged values of HONO/NO_2 were 0.011±0.004, 0.014±0.006, 0.008±0.003, and
332 0.007±0.003 when aerosol extinctions are 0–0.3, 0.3–0.6, 0.6–0.9 and > 0.9 km^{-1} in the inland case, respectively
333 (Figure 8(b)). As shown in Figure 8, the high values of HONO/NO_2 were mainly under aerosol extinction being less
334 than 1.0 km^{-1} with averaged values of 0.012±0.006 and 0.090±0.004 in the coastal and sea cases, respectively. It
335 indicates that aerosol surface plays a more important role in forming HONO through NO_2 heterogeneous reaction in
336 the sea condition than that in the land condition.

3.3 Vertical distributions of HONO/NO_2 under different aerosol condition in land and sea

338 To further investigate the height dependence of HONO/NO_2 under land and sea conditions, two cases in Pearl River
339 Delta (PRD) were selected from the whole campaign. As shown in Figure 9, "A" and "B" were under similar aerosol
340 level (the extinction coefficients in surface layer being 0.45–0.60 km^{-1}) and vertical distribution structure, and were all
341 observed from 10:00 to 11:00 hrs. The instrument viewed sea accompanied with sea wind in "A" named sea scene,
342 and the instrument viewed land accompanied with land wind in "B" named land scene. The NO_2 in the sea and land
343 scenes have a similar vertical structure, and the NO_2 concentration in land scene are larger than that in sea scene
344 except on the surface layer. The HONO have the same vertical distribution structure in the above two scenes, and the
345 HONO concentration in the land scene is always larger than that in the sea scene. In Figure 9(e), we found that
346 HONO/NO_2 under 0–400 m in the land scene is higher than that in the sea scene, however, the HONO/NO_2 values are
347 obviously lower in the land scene than that in the sea scene above 400 m. Furthermore, the growth rate of HONO/NO_2
348 with the increase of height in the sea scene is significantly faster than that in the land scene above 400 m. This
349 indicates the generation rates of HONO sourced from NO_2 heterogeneous reaction on aerosol surface in the sea scene
350 is larger than that in the land scene above 400 m. Under 400 m, the HONO generation rates in the land scene is larger
351 than that in the sea scene.

352 Additionally, we selected inland cases (CAMS) to learn the difference of height dependence of HONO/NO_2 compared
353 with sea scenes under different aerosol loads. As shown in Figure 10, the sea and inland scenes had similar aerosol
354 levels (low aerosol level: < 0.2 km^{-1}) and vertical structure. Furthermore, the NO_2 and HONO in the sea and inland
355 scenes have similar vertical structure, although their concentrations in the sea scene are all larger than that in the
356 inland scene. In Figure 10(d), we found that the HONO/NO_2 in the sea scene was obviously larger than that in the
357 inland scene above 400 m. The HONO/NO_2 in the sea scene was about 4.5 times larger than that in the inland scene
358 especially above 600 m. As shown in Figure 11, the aerosols under the sea and inland scenes exhibited similar
359 extinction levels (relatively high level: ~0.8 km^{-1}) and vertical structure. The NO_2 concentration in the sea scene was
360 higher than that in the inland scene but with a similar vertical structure. The HONO concentration in the sea scene was
361 lower than that in the inland scene under 400 m, while the concentration in the sea scene was larger than that in the
362 inland scene above 400 m. In Figure 11 (d), we found the HONO/NO_2 in the inland scene was larger than that in the
363 sea scene under 600 m, while the HONO/NO_2 in the sea scene was about 2 times larger than that in the inland scene
364 above 600 m. All the above cases indicated that the HONO generation rate from NO_2 heterogeneous reaction in the
365 sea scene was larger than that in the inland scene in higher atmospheric layers above 400–600 m. The high-altitude (>
366 400–600 m) atmospheric parameters in the sea scene were more conductive to promote the HONO formation through
367 the heterogeneous reaction of NO_2. As shown in Figure S9, the ratio of HONO/NO_2 also generally increased with the
368 increase in height above 0.2 km during the whole ship-based campaign. The greatest sensitivity under 1.5 km and the
369 high degree of freedom (DOF) for aerosol, NO_2, and HONO gave confidence in the retrieval results (Figure S10).

3.4 Case study

371 The important factors and precursors to drive the formation of HONO through heterogeneous reaction had complex
372 evolution and transport characteristics. To further clarify the role of these parameters in the heterogeneous process of
373 NO_2 to form HONO, three typical processes were selected to reveal the favorable conditions for HONO formation at
374 the sea scene.

3.4.1 20 April: A typical transport event

As shown in Figure 12, the aerosol mainly distributed in 0–200 m with a mean extinction coefficient larger than 0.74 km^{-1}. NO$_2$ was mainly distributed near the ground surface with a mean concentration of 28.54 ppb before 13:20. The NO$_2$ during this period may come from local ship emissions, as this area is a main shipping channel. From 14:25 to 17:10, a high-concentration NO$_2$ air mass (averaged 13.29 ppb) was found at ~2.0 km. To understand the source of this high-altitude NO$_2$ air mass, we further investigated the possible influence of transport by using the backward trajectories. We calculated 24 h backward trajectories of air masses at 500, 1000, and 2000 m using HYSPLIT (Figure S11). In Figure S11, we found that the dominant wind direction during this period was southeast at all heights, i.e., 500, 1000, and 2000 m. The transport of air masses carried NO$_2$ emitted by ships in Ningbo and Zhoushan ports to main cargo ports of China and Shanghai. Furthermore, the concentration of NO$_2$ was low (averaged 2.32 ppb) near the ground surface from 14:25 to 17:10. As shown in Figure 12 (e) and (g), a low pressure (< 1020 hPa), north dominant wind direction with the wind speed > 12 m/s appeared at the ground surface during this period, which implies that the clean air from north reduced the local surface NO$_2$. The HONO was mainly distributed near the surface with a mean concentration of 0.07 ppb, and the two peaks were found in the early morning (averaged 0.15 ppb) and at 12:15 (averaged 0.11 ppb), respectively (Figure S12). The relatively high concentration of HONO appearing in the early morning was possibly attributed to the accumulation with the stabilization of boundary layer and attenuation of solar radiation after sunset the day before (Xing et al., 2021). The HONO peak appearing at 12:15 may be sourced from the heterogeneous reaction of NO$_2$ on the aerosol surface under a ~80% RH, 18.5℃ temperature, and 1×10^3 W/m^2 SRI conditions.

3.4.2 28 April: A typical event of HONO produced from NO$_2$ heterogeneous reaction

From a typical port observation case, the measurement ship moored at Xiamen port on 28 April. As shown in Figure 13, we found two peaks for aerosol and NO$_2$ from 09:00–11:00 and 14:00–16:00, respectively (averaged aerosol extinction coefficient > 0.8 km^{-1}, averaged NO$_2$ concentration > 12.0 ppb). NO$_2$ was mainly distributed near the sea surface layer 0–200 m, and a high-concentration NO$_2$ air mass was found from 1.0–2.0 km during 13:00–14:00 due to the short distance transport of NO$_2$ emitted from ships in Xiamen port (Figure S13). However, aerosol appeared in the range of 0.0–2.0 km during 09:00–11:00 and 14:00–16:00. In Figure 13 (g), we found that the wind speeds in the above two peak periods were obviously higher than that in other periods. From 09:00–11:00, the wind speed was ~5.0 m/s with a northwest dominant direction (urban), and the wind speed was ~6.0 m/s with a southeast dominant direction (port gateway) during 14:00–16:00, which indicates that the short-distance high-altitude transport caused the appearance of high-extinction aerosol mass during the above two periods.

Furthermore, we found the high-concentration HONO only appeared at 14:00–16:00 with a 0.57 ppb averaged concentration under 0.9 km, while it was only about 0.14 ppb during 09:00–11:00 period. The slight increase of RH and temperature (Tem) at 14:00–16:00 (RH: ~75.0%, Tem: 23.7℃) may contribute to HONO formation through heterogeneous reaction of NO$_2$ on the aerosol surface than that at 09:00–11:00 (Figure 13 (d)-(e), Section 3.2). Contrarily, the solar radiation intensity (SRI) (~600 W/m^2) at 09:00-11:00 was obviously larger than that (~250 W/m^2) at 14:00–16:00 (Figure 13 (f)). The higher SRI accelerated the photolysis of HONO during 09:00-11:00 period (Kraus et al., 1998). Therefore, the lower formation rate and higher photolysis rate lead to a significantly lower HONO concentration at 09:00-11:00 than that at 14:00-16:00.

3.4.3 03 May: A typical event with unknown HONO source

The measurement ship conducted observation in the sea area near Zhanjiang on 03 May, 2018. As shown in Figure 14, we found that there was an obvious sinking process for aerosol from ~1.0 km during 09:00-16:00, and eventually accumulated near the sea surface with a high extinction coefficient > 0.92 km^{-1}. The NO$_2$ was mainly concentrated near the sea surface layer (0–400 m) with an averaged concentration of 8.93 ppb from 08:00 to 09:00. Thereafter, with the rise the planetary boundary layer (PBL) height after sunrise, NO$_2$ was gradually mixed and spread throughout the PBL from 09:00–13:00. During this period, it was accompanied by the increase of the NO$_2$ concentration (averaged 11.2 ppb) under PBL (Figure S14). It is due to the contribution of ship emissions near the sea surface. Contrarily, the regional transport of NO$_2$ from land also increased the NO$_2$ concentration in this area of the sea, with wind speed increasing from 2.5 to 7.8 m/s with a north wind direction from 10:00 to 16:00 (Figure 14 (g)).

Several HONO peaks (> 0.2 ppb) at 0.5–1.0 km were found from 09:45 to 13:00, and the aerosol and NO$_2$ high values were also observed at this height layer, simultaneously, which implies that the heterogeneous reaction of NO$_2$ on aerosol surface is more important than that on the sea surface for HONO source under sea atmosphere. Additionally, HONO concentration obviously elevated after 14:00, especially during 14:00–16:00 (> 0.4 ppb). It may be sourced from heterogeneous reaction of NO$_2$ on the aerosol surface, under RH a being ~92.5% (Figure 14 (d)). The photolysis of HONO also decreased with SRI < 150 W/m^2 (Figure 14 (f)) during this period. Furthermore, a HONO peak (> 0.32 ppb) was observed during 16:40–17:10. However, the NO$_2$ concentration always kept low (< 1.5 ppb) after 16:00, and the temperature was lower than 17 ℃ (Figure 14 (e)), which indicates the heterogeneous reaction of NO$_2$ not being the source of the observed HONO peak. The wind was north dominant with an average speed at 7.8 m/s after 15:00,

8

which implies that the regional transport may not be the source of the observed high-concentration of HONO. Furthermore, the SRI was lower than 87.5 W/m^2, and it shows the photolysis of nitrate aerosol also not being the source of the elevated HONO. The unknown HONO source in this area of the sea need to be further explored.

4 Summary and Conclusions

Currently, many uncertainties in the study of the HONO forming mechanism through the heterogeneous reaction of NO$_2$ exist. Earlier studies mostly focused on the near-surface layer, and the assessment of the contribution of NO$_2$ heterogeneous reaction to HONO formation in the vertical direction of the boundary layer is insufficient. Therefore, we aim to learn the sea-land and vertical differences of the HONO forming mechanism from NO$_2$ heterogeneous reaction and provide deep insights into the distribution characteristics, transforming process, and environmental effects of tropospheric HONO. Ship based MAX-DOAS observations along the marginal seas of China were performed from 19 April to 16 May 2018. Simultaneously, two ground-based MAX-DOAS observations were conducted in the inland station CAMS and the coastal station SUST to measure the aerosol, NO$_2$, and HONO vertical profiles.

Along the cruise route, we found five hot spots with enhanced tropospheric NO$_2$ VCDs in Yangtze River Delta, Taiwan straits, Guangzhou-Hong Kong-Macao Greater Bay areas, Zhanjiang Port, and Qingdao port. Under high-level NO$_2$ conditions in the above five hot spots, we also observed enhanced HONO levels. Contrastingly, the low-concentration HONO accompanied high-level NO$_2$ in the southeast coastline of Jiangsu province. When peak AOD and NO$_2$ conditions were observed, enhanced HONO were observed, although the reverse was not always the case.

To understand the impacts of RH, temperature, and aerosol on the heterogeneous reaction of NO$_2$ to produce HONO, the emission ratios of ΔHONO/ΔNOx were calculated to quantify the contribution of the primary HONO source to the total production of HONO. We found that the RH turning points in CAMS and SUST cases were both ~65% (60–70%), whereas two turning peaks (~60% and ~85%) of RH were found in the sea cases. This implied that high RH could contribute to the secondary formation of HONO in sea atmosphere. With increase in temperature, the HONO/NO$_2$ decreased with peak values appearing at ~12.5℃ in CAMS, whereas the HONO/NO$_2$ gradually increased and reached peak values at ~31.5℃ in SUST. In the sea case, when the temperature exceeded 18.0℃, the HONO/NO$_2$ increased with the increasing temperature and achieved peak at ~25.0℃. This indicated that high temperature could promote the secondary formation of HONO in the sea and coastal atmosphere. Additionally, the correlation analysis under different sea-land conditions indicated that the ground surface is more crucial to the formation of HONO from NO$_2$ heterogeneous reaction in the inland case, whereas the aerosol surface contributed more in the coastal and sea cases.

Furthermore, we found that the HONO/NO$_2$ in the sea case was about 4.5 times larger than that in the inland case above 600 m when AEC was ~0.2 km^{-1}, and the HONO/NO$_2$ ratio in the sea case was about 2 times larger than that in the inland case above 600 m when AEC was ~0.8 km^{-1}, which implied that the generation rate of HONO from NO$_2$ heterogeneous reaction in the sea case is larger than that in the inland case in higher atmospheric layers (> 600 m). To have a deep understanding of three potential contributing factors of HONO production under marine condition, we selected three typical events, which represented the impacts of transport, NO$_2$ heterogeneous reaction, and unknown HONO source, respectively.

Data availability

All measurement data used in this study can be made available for scientific purpose upon request to the corresponding author (chliu81@ustc.edu.cn).

Author contributions

CX, CL and KL designed the research and organized this paper. CX wrote this paper, and CL and KL edited it. CX, SX, and YS contributed to the retrieval of MAX-DOAS vertical-profile data. CX, YL CZ, QH and SW contributed to data analysis. CX, WT, HW and HL contributed to the MAX-DOAS instrument setup and observations. All above authors contributed to the revision of this manuscript.

Competing interests

We declared that none of the authors has any competing interests.

Acknowledgements

486 We would like to also thank Fudan University (Professor Jianmin Chen's group) for organizing the ship-based
487 campaign and providing meteorological data.

488

495

496 **References**
497 Alicke, B., Geyer, A., Hofzumahaus, A., Holland, F., Konrad, S., Patz, H. W., Schafer, J., Stutz, J., Volz-Thomas, A.,
498 Platt, U.: OH formation by HONO photolysis during the BERLIOZ experiment, J. Geophys. Res.-Atmos., 2003, 108,
499 8247.
500 Aliwell, S., Van Roozendael, M., Johnston, P., Richter, A., Wagner, T., Arlander, D. W., Burrows, J. P., Fish, D. J.,
501 Jones, R. L., Tornkvist, K. K., Lambert, J. C., Pfeilsticker, K., Pundt, I.: Analysis for BrO in zenith-sky spectra: an
502 Intercomparison exercise for analysis improvement. J. Geophys. Res., 2002, 107, 4199.
503 Bernard, F., Cazaunau, M., Grosselin, B., Zhou, B., Zheng, J., Liang, P., Zhang, Y., Ye, X., Daele, V., Mu, Y., Zhang,
504 R., Chen, J., Mellouki, A.: Measurements of nitrous acid (HONO) in urban area of Shanghai, China. Environ. Sci.
505 Pollut. Res., 2016, 23:5818–5829.
506 Cheng, P., Cheng, Y., Lu, K., Su, H., Yang, Q., Zou, Y., Zhao, Y., Dong, H., Zeng, L., Zhang, Y.: An online
507 monitoring system for atmospheric nitrous acid (HONO) based on stripping coil and ion chromatography. J. Environ.
508 Sci., 2013, 25(5) 895–907.
509 Cui, L., Li, R., Fu, H., Li, Q., Zhang, L., George, C., Chen, J.: Formation features of nitrous acid in the offshore area
510 of the East China Sea. Sci. Total Environ., 2019, 682, 138–150.
511 Cui, L., Li, R., Zhang, Y., Meng, Y., Fu, H., Chen, J.: An observational study of nitrous acid (HONO) in Shanghai,
512 China: The aerosol impact on HONO formation during the haze episodes. Sci. Total Environ., 2018, 630, 1057–1070.
513 Fleischmann, O. C., Hartmann, M., Burrows, J. P., Orphal, J.: New ultraviolet absorption cross-sections of BrO at
514 atmospheric temperatures measured by time-windowing Fourier transform spectroscopy. J. Photoch. Photobio., 2004,
515 A 168, 117–132.
516 Fu, X., Wang, T., Zhang, L., Li, Q., Wang, Z., Xia, M., Yun, H., Wang, W., Yu, C., Yue, D., Zhou, Y., Zheng, J., Han,
517 R.: The significant contribution of HONO to secondary pollutants during a severe winter pollution event in southern
518 China. Atmos. Chem. Phys., 2019, 19, 1–14.
519 Garcia-Nieto, D., Benavent, N., Saiz-Lopez, A.: Measurements of atmospheric HONO vertical distribution and
520 temporal evolution in Madrid (Spain) using the MAX-DOAS technique. Sci. Total Environ., 2018, 643, 957–966.
521 Gil, G., Kim, J., Lee, M., Lee, G., Lee, D., Jung, J., An, J., Hong, J., Cho, S., Lee, J., Long, R.: The role of HONO in
522 O3 formation and insight into its formation mechanism during the KORUS-AQ Campaign. Atmos. Chem. Phys.
523 Discus., 2019, https://doi.org/10.5194/acp-2019-1012.
524 Guo, Y., Wang, S., Gao, S., Zhang, R., Zhu, J., Zhou, B.: Influence of ship direct emission on HONO sources in
525 channel environment. Atmos. Environ., 2020, 242, 117819.
526 He, S., Wang, S., Zhang, S., Zhu, J., Sun, Z., Xue, R., Zhou, B.: Vertical distributions of atmospheric HONO and the
527 corresponding OH radical production by photolysis at the suburb area of Shanghai, China, Sci. Total Environ., 2023,
528 858, 159703.
529 Huang, R., Yang, L., Cao, J., Wang, Q., Tie, X., Ho, K. F., Shen, Z., Zhang, R., Li, G., Zhu, C., Zhang, N., Dai, W.,
530 Zhou, J., Liu, S., Chen, Y., Chen, J., O'Dowd, C. D.: Concentration and sources of atmospheric nitrous acid (HONO)
531 at an urban site in Western China. Sci. Total Environ., 2017, 593–594, 165–172.
532 Huang, R., Zhang, Y., Bozzetti, C., Ho, K. F., Cao, J. J., Han, Y., Daellenbach, K. R., Slowik, J. G., Platt, S. M.,
533 Canonaco, F., Zotter, P., Wolf, R., Pieber, S. M., Bruns, E. A., Crippa, M., Ciarelli, G., Piazzalunga, A., Schwikowski,
534 M., Abbaszade, G., Schnelle-Kreis, J., Zimmermann, R., An, Z., Szidat, S., Baltensperger, U., Haddad, I. E., Prevot,
535 A. S. H.: High secondary aerosol contribution to particulate pollution during haze events in China. Nature, 2014, 514,
536 218-222.
537 Indarto, A.: Heterogeneous reactions of HONO formation from NO_2 and HNO_3: a review, 2012, 38, 1029-1041.
538 Jordan, N., Osthoff, H. D.: Quantification of nitrous acid (HONO) and nitrogen dioxide (NO_2) in ambient air by
539 broadband cavity-enhanced absorption spectroscopy (IBBCEAS) between 361 and 388 nm. Atmos. Meas. Tech.,
540 2020, 13, 273–285.
541 Kleffmann, J., Gavriloaiei, T., Hofzumahaus, A., Holland, F., Koppmann, R., Rupp, L., Schlosser, E., Siese, M.,
542 Wahner, A.: Daytime formation of nitrous acid: A major source of OH radicals in a forest, Geophys. Res. Lett., 2005,
543 32, L05818.

Kleffmann, J., Kurtenbach, R., Lorzer, J., Wiesen, P., Kalthoff, N., Vogel, B., Vogel, H.: Measured and simulated vertical profiles of nitrous acid-Part I: Field measurements, Atmos. Environ., 2003, 37, 2949-2955.

Kraus, A., Hofzumahaus, A.: Field Measurements of Atmospheric Photolysis Frequencies for O_3, NO_2, HCHO, CH_3CHO, H_2O_2, and HONO by UV Spectroradiometry. Atmospheric Measurements during POPCORN—Characterisation of the Photochemistry over a Rural Area, Springer, 1998: 161-180.

Liu, C., Xing, C., Hu, Q., Li, Q., Liu, H., Hong, Q., Tan, W., Ji, X., Lin, H., Lu, C., Lin, J., Liu, H., Wei, S., Chen, J., Yang, K., Wang, S., Liu, T., Chen, Y.: Ground-based hyperspectral stereoscopic remote sensing network: A promising strategy to learn coordinated control of O_3 and $PM_{2.5}$ over China. Engineering, 2022, 19, 71-83.

Liu, J., Liu, Z., Ma, Z., Yang, S., Yao, D., Zhao, S., Hu, B., Tang, G., Sun, J., Cheng, M., Xu, Z., Wang, Y.: Detailed budget analysis of HONO in Beijing, China: Implication on atmosphere oxidation capacity in polluted megacity. Atmos. Environ., 2021, 244, 117957.

Liu, Y., Nie, W., Xu, Z., Wang, T., Wang, R., Li, Y., Wang, L., Chi, X., Ding, A.: Semi-quantitative understanding of source contribution to nitrous acid (HONO) based on 1 year of continuous observation at the SORPES station in eastern China. Atmos. Chem. Phys., 2019, 19, 13289–13308.

Liu, Y., Nie, W., Xu, Z., Wang, T., Wang, R., Li, Y., Wang, L., Chi, X., and Ding, A.: Contributions of different sources to nitrous acid (HONO) at the SORPES station in eastern China: results from one-year continuous observation. Atmos. Chem. Phys. Discuss., 10.5194/acp-2019-219, 2019.

Meller, R., Moortgat, G. K.: Temperature dependence of the absorption cross sections of formaldehyde between 223 and 323 K in the wavelength range 225–375 nm. J. Geophys. Res., 2000, 105, 7089–7101.

Meng, F., Qin, M., Tang, K., Duan, J., Fang, W., Liang, S., Ye, K., Xie, P., Sun, Y., Xie, C., Ye, C., Fu, P., Liu, J., Liu, W.: High-resolution vertical distribution and sources of HONO and NO_2 in the nocturnal boundary layer in urban Beijing, China. Atmos. Chem. Phys., 2020, 20, 5071–5092.

Michoud, V., Kukui, A., Camredon, M., Colomb, A., Borbon, A., Miet, K., Aumont, B., Beekmann, M., Durand-Jolibois, R., Perrier, S., Zapf, P., Siour, G., Ait-Helal, W., Locoge, N., Sauvage, S., Afif, C., Gros, V., Furger, M., Ancellet, G., Doussin, J. F.: Radical budget analysis in a suburban European site during the MEGAPOLI summer field campaign. Atmos. Chem. Phys., 2012, 12, 11951–11974.

Rodgers, C. D., Taylor, F. W. (Ed.): Inverse methods for atmospheric sounding, theory and practice, World Scientific, 255 pp.2004.

Rothman, L., Gordon, I., Barber, R., Dothe, H., Gamache, R. R., Goldman, A., Perevalov, Tashkun, S. A., Tennyson, J.: HITEMP, the high-temperature molecular spectroscopic database. J. Quant. Spectrosc. Ra., 2010, 111, 2139–2150.

Ryan, R. G., Rhodes, S., Tully, M., Wilson, S., Jones, N., Frieß, U., Schofield, R.: Daytime HONO, NO_2 and aerosol distributions from MAX-DOAS observations in Melbourne. Atmos. Chem. Phys., 2018, 18, 13969–13985.

Salgado, M. S., and Rossi, M. J.: Flame soot generated under controlled combustion conditions: Heterogeneous reaction of NO_2 on hexane soot, International Journal of Chemical Kinetics, 34, 620-631, 10.1002/kin.10091, 2002.

Serdyuchenko, A., Gorshelev, V., Weber, M., Chehade, W., Burrows, J. P.: High spectral resolution ozone absorption cross-sections –part 2: temperature dependence. Atmos. Meas. Tech., 2014, 7, 625–636.

Song, Y., Xing, C., Liu, C., Lin, J., Wu, H., Liu, T., Lin, H., Zhang, C., Tan, W., Ji, X., Liu, H., Li, Q.: Evaluation of transport processes over North China Plain and Yangtze River Delta using MAX-DOAS observations. Atmos. Chem. Phys., 2023, 23, 1803-1824.

Stemmler, K., Ammann, M., Donders, C., Kleffmann, J., George, C.: Photosensitized reduction of nitrogen dioxide on humic acid as a source of nitrous acid, nature, 2006, 440, 195-198.

Stutz, J., Kim, E. S., Platt, U., Bruno, P., Perrino, C., Febo, A.: UV–visible absorption cross sections of nitrous acid. J. Geophys. Res.-Atmos., 2000, 105, 14585–14592.

Sun, L., Chen, T., Jiang, Y., Zhou, Y., Sheng, L., Lin, J., Li, J., Dong, C., Wang, C., Wang, X., Zhang, Q., Wang, W., Xue, L.: Ship emission of nitrous acid (HONO) and its impacts on the marine atmospheric oxidation chemistry. Sci. Total Environ., 2020, 735, 139355.

Tan, W., Liu, C., Wang, S., Xing, C., Su, W., Zhang, C., Xia, C., Liu, H., Cai, Z., Liu, J.: Tropospheric NO_2, SO_2, and HCHO over the East China Sea, using ship-based MAX-DOAS observations and comparison with OMI and OMPS satellite data. Atmos. Chem. Phys., 2018, 18, 15387–15402.

Thalman, R., Volkamer, R.: Temperature dependent absorption cross-sections of O_2–O_2 collision pairs between 340 and 630 nm and at atmospherically relevant pressure. Phys. Chem. Chem. Phys., 2013, 15, 15371–15381.

Vandaele, A. C., Hermans, C., Simon, P. C., Carleer, M., Colin, R., Fally, S., Merienne, M. F., Jenouvrier, A., Coquart, B.: Measurements of the NO_2 absorption cross-section from 42,000 cm^{-1} to 10,000 cm^{-1} (238–1000 nm) at 220K and 294 K. J. Quant. Spectrosc. Ra., 1998, 59, 171–184.

Wang, L., Wen, L., Xu, C., Chen, J., Wang, X., Yang, L., Wang, W., Yang, X., Sui, X., Yao, L., Zhang, Q.: HONO and its potential source particulate nitrite at an urban site in North China during the cold season. Sci. Total Environ., 2015, 538, 93–101.

Wang, Y., Apituley, A., Bais, A., Beirle, S., Benavent, N., Borovski, A., Bruchkouski, I., Chan, K. L., Donner, S., Drosoglou, T., Finkenzeller, H., Friedrich, M. M., Frieß, U., Garcia-Nieto, D., Gómez-Martín, L., Hendrick, F., Hilboll, A., Jin, J., Johnston, P., Koenig, T. K., Kreher, K., Kumar, V., Kyuberis, A., Lampel, J., Liu, C., Liu, H., Ma, J., Polyansky, O. L., Postylyakov, O., Querel, R., Saiz-Lopez, A., Schmitt, S., Tian, X., Tirpitz, J.-L., Roozendael, M.

605 V., Volkamer, R., Wang, Z., Xie, P., Xing, C., Xu, J., Yela, M., Zhang, C., Wagner, T.: Inter-comparison of
606 MAX-DOAS measurements of tropospheric HONO slant column densities and vertical profiles during the CINDI-2
607 campaign, Atmos. Meas. Tech., 2020, 13, 5087-5116.
608 Wang, Y., Dörner, S., Donner, S., Bohnke, S., Smedt, I. D., Dickerson, R. R., Dong, Z., He, H., Li, Z., Li, Z., Li, D.,
609 Liu, D., Ren, X., Theys, N., Wang, Y., Wang, Y., Wang, Z., Xu, H., Xu, J., Wagner, T.: Vertical profiles of NO_2, SO_2,
610 HONO, HCHO, CHOCHO and aerosols derived from MAX-DOAS measurements at a rural site in the central
611 western North China Plain and their relation to emission sources and effects of regional transport. Atmos. Chem.
612 Phys., 2019, 19, 5417–5449.
613 Wang, Y., Lampel, J., Xie, P., Beirle, S., Li, A., Wu, D., and Wagner, T.: Ground-based MAX-DOAS observations of
614 tropospheric aerosols, NO_2, SO_2 and HCHO in Wuxi, China, from 2011 to 2014, Atmos. Chem. Phys., 17, 2189-2215,
615 10.5194/acp-17-2189-2017, 2017.
616 Wen, L., Chen, T., Zheng, P., Wu, L., Wang, X., Mellouki, A., Wang, W.: Nitrous acid in marine boundary layer over
617 eastern Bohai Sea, China: Characteristics, sources, and implications. Sci. Total Environ., 2019, 670, 282–291.
618 Wong, K. W., Tsai, C., Lefer, B., Haman, C., Grossberg, N., Brune, W. H., Ren, X., Luke, W., Stutz, J.: Daytime
619 HONO vertical gradients during SHARP 2009 in Houston, TX, Atmos. Chem. Phys., 2012, 12, 635-652.
620 Xing, C., Liu, C., Hu, Q., Fu, Q., Lin, H., Wang, S., Su, W., Wang, W., Javed, Z., Liu, J.: Identifying the wintertime
621 sources of volatile organic compounds (VOCs) from MAX-DOAS measured formaldehyde and glyoxal in Chongqing,
622 southwest China. Sci. Total Environ., 2020, 715, 136258.
623 Xing, C., Liu, C., Hu, Q., Fu, Q., Wang, S., Lin, H., Zhu, Y., Wang, S., Wang, W., Javed, Z., Ji, X., Liu, J.: Vertical
624 distributions of wintertime atmospheric nitrogenous compounds and the corresponding OH radicals production in
625 Leshan, southwest China. J. Environ. Sci., 2021, 105, 44–55.
626 Xing, C., Liu, C., Wang, S., Chan, K. L., Gao, Y., Huang, X., Su, W., Zhang, C., Dong, Y., Fan, G., Zhang, T., Chen,
627 Z., Hu, Q., Su, H., Xie, Z., Liu, J.: Observations of the vertical distributions of summertime atmospheric pollutants
628 and the corresponding ozone production in Shanghai, China. Atmos. Chem. Phys. 2017, 17, 14275–14289.
629 Xing, C., Li, C., Wang, S., Hu, Q., Liu, H., Tan, W., Zhang, W., Li, B., Liu, J.: A new method to determine the
630 aerosol optical properties from multiple-wavelength O_4 absorptions by MAX-DOAS observation. Atmos. Meas. Tech.,
631 2019, 12, 3289–3302.
632 Xue, C., Zhang, C., Ye, C., Liu, P., Catoire, V., Krysztofiak, G., Chen, H., Ren, Y., Zhao, X., Wang, J., Zhang, F.,
633 Zhang, C., Zhang, J., An, J., Wang, T., Chen, J., Kleffmann, J., Mellouki, A., Mu, Y.: HONO Budget and Its Role in
634 Nitrate Formation in the Rural North China Plain. Environ. Sci. Technol., 2020, 54, 11048-11057.
635 Xu, S., Wang, S., Xia, M., Lin, H., Xing, C., Ji, X., Su, W., Tan, W., Liu, C., Hu, Q.: Observations by ground-based
636 MAX-DOAS of the vertical characters of winter pollution and the influencing factors of HONO generation in
637 Shanghai, China, Remote Sens., 2021, 13(17), 3518.
638 Xu, Z., Wang, T., Wu, J., Xue, L., Chan, J., Zha, Q., Zhou, S., Louie, P. K. K., Luk, C. W. Y.: Nitrous acid (HONO)
639 in a polluted subtropical atmosphere: Seasonal variability, direct vehicle emissions and heterogeneous production at
640 ground surface, Atmos. Environ., 2015, 106, 100–109.
641 Yang, Y., Li, X., Zu, K., Lian, C., Chen, S., Dong, H., Feng, M., Liu, H., Liu, J., Lu, K., Li, S., Ma, X., Song, D.,
642 Wang, W., Yang, S., Yang, X., Yu, X., Zhu, Y., Zeng, L., Tan, Q., Zhang, Y.: Elucidating the effect of HONO on O_3
643 pollution by a case study in southwest China. Sci. Total Environ., 2021, 756, 144127.
644 Zhang, B., Wang, Y., Hao, J.: Simulating aerosol-radiation-cloud feedbacks on meteorology and air quality over
645 eastern China under severe haze conditions in winter. Atmos. Chem. Phys., 2015, 15, 2387–2404.
646 Zhang, N., Zhou, X., Shepson, P. B., Gao, H., Alaghmand, M., Stirm, B.: Aircraft measurement of HONO vertical
647 profiles over a forested region, Geophys. Res. Lett., 2009, 36(15), L15820.
648 Zhang, W., Tong, S., Jia, C., Wang, L., Liu, B., Tang, G., Ji, D., Hu, B., Liu, Z., Li, W., Wang, Z., Liu, Y., Wang, Y.,
649 Ge, M.: Different HONO Sources for Three Layers at the Urban Area of Beijing. Environ. Sci. Technol., 2020, 54,
650 12870-12880.
651 Zha, Q., Xue, L., Wang, T., Xu, Z., Yeung, C., Louie, P. K. K., Luk, C. W. Y.: Large conversion rates of NO_2 to
652 HNO_2 observed in air masses from the South China Sea: Evidence of strong production at sea surface? Geophys. Res.
653 Lett., 2014, 41, 7710–7715.
654 Zhou, X., Zhang, N., TerAvest, M., Tang, D., Hou, J., Bertman, S., Alaghmand, M., Shepson, P. B., Carroll, M. A.,
655 Griffith, S., Dusanter, S., and Stevens, P. S.: Nitric acid photolysis on forest canopy surface as a source for
656 tropospheric nitrous acid, Nature Geoscience, 4, 440-443, 10.1038/ngeo1164, 2011.
657
658
659
660
661

662

Table 1. Detailed information of the measurement cruise

Cruise NO.	Periods	Measurement cruise
NO. 1	08:50 to 21:02 19 Apr.	Daishan port (30.24ºN, 122.16ºE) to Chongming (31.18ºN, 121.82ºE)
NO. 2	05:40 to 17:45 20 Apr.	Sailing around Chongming island
NO. 3	06:03 21 Apr. to 08:07 03 May	Chongming (31.18ºN, 121.82ºE) to Zhanjiang port (21.12ºN, 110.67ºE)
NO. 4	08:07 03 May to 06:52 09 May	Zhanjiang port (21.12ºN, 110.67ºE) to Daishan port (30.24ºN, 122.16ºE)
NO. 5	05:40 11 May to 05:55 14 May	Daishan port (30.24ºN, 122.16ºE) to Qingdao (35.89ºN, 120.87ºE)
NO. 6	05:55 14 May to 10:00 16 May	Qingdao (35.89ºN, 120.87ºE) to Daishan port (30.24ºN, 122.16ºE)

663
664

Table 2. Detailed retrieval settings of O_4, NO_2, and HONO.

Parameter	Data source	Fitting internals (nm)		
		O_4	NO_2	HONO
Wavelength range		338-370	338-370	335-373
NO_2	298K, I_0-corrected, Vandaele et al. (1998)	√	√	√
NO_2	220K, I_0-corrected, Vandaele et al. (1998)	√	√	√
O_3	223K, I_0-corrected, Serdyuchenko et al. (2014)	√	√	√
O_3	243K, I_0-corrected, Serdyuchenko et al. (2014)	√	√	√
O_4	293K, Thalman and Volkamer (2013)	√	√	√
HCHO	298K, Meller and Moortgat (2013)	√	√	√
H_2O	HITEMP (Rothman et al. 2010)	×	×	√
BrO	223K, Fleischmann et al. (2004)	√	√	√
HONO	296K, Stutz et al. (2000)	×	×	√
Ring	Calculated with QDOAS	√	√	√
Polynomial degree		Order 5	Order 5	Order 5
Intensity offset		Constant	Constant	Constant

665
666
* Solar I_0 correction; Aliwell et al. (2002).

667

Table 3. Error budget estimation (in %) of the retrieved near-surface (0–200 m) trace gas concentrations and AECs, and trace gas VCDs and AOD.

			Error source				Total
			Smoothing and noise errors	Algorithm error	Cross section error	Related to the aerosol retrieval (only for trace gases)	
Cruise route	Near-surface	aerosol	14	4	4	-	15
		NO_2	16	3	3	15	22
		HONO	20	20	5	15	32
	VCD or AOD	AOD	5	8	4	-	10
		NO_2	17	11	3	10	23
		HONO	22	20	5	10	32
SUST	Near-surface	aerosol	13	4	4	-	14
		NO_2	14	3	3	14	20
		HONO	18	20	5	14	31
	VCD or AOD	AOD	5	8	4	-	10
		NO_2	16	11	3	10	22
		HONO	20	20	5	10	30
CAMS	Near-surface	aerosol	13	4	4	-	14
		NO_2	15	3	3	14	21
		HONO	19	20	5	14	31
	VCD or AOD	AOD	5	8	4	-	10
		NO_2	17	11	3	10	23
		HONO	21	20	5	10	31

670
671

14

672
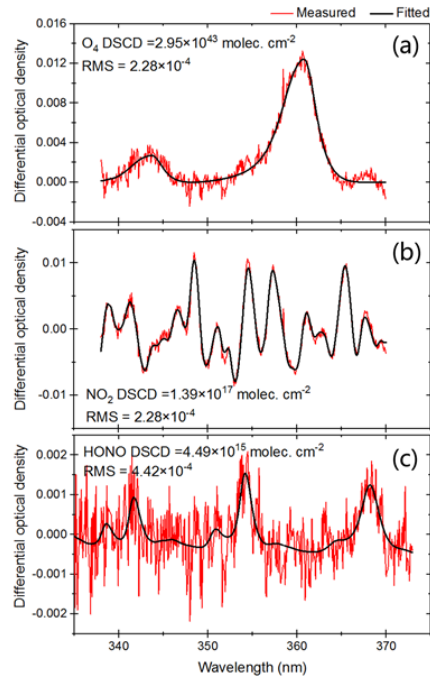
673
674   Figure 1. Plots depicting typical DOAS spectral fittings for (a) O_4, (b) NO_2 and (c) HONO.

675
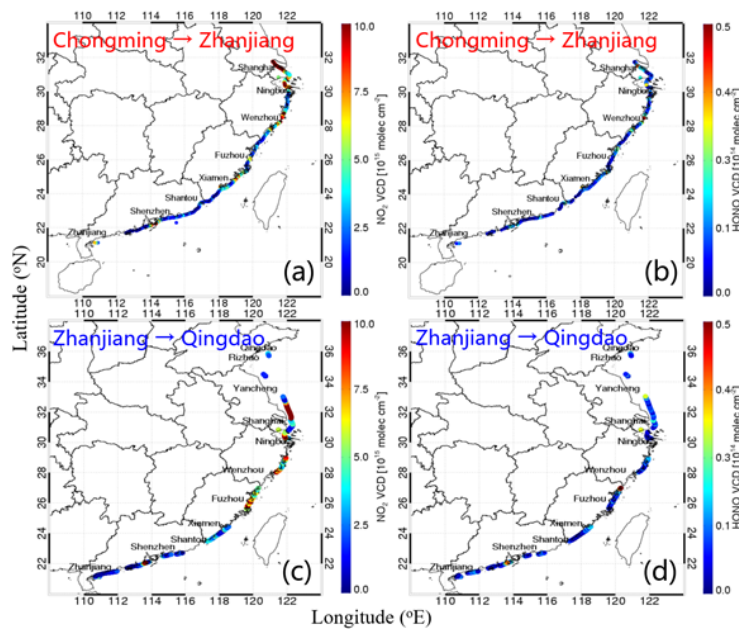
676
677   Figure 2. Maps showing the spatial distributions of NO_2 and HONO VCDs. (a) and (b) show the NO_2 and HONO
678   VCDs along the cruise route from Chongming to Zhanjiang. (c) and (d) depict the NO_2 and HONO VCDs along the
679   cruise route from Zhanjiang to Qingdao.

680
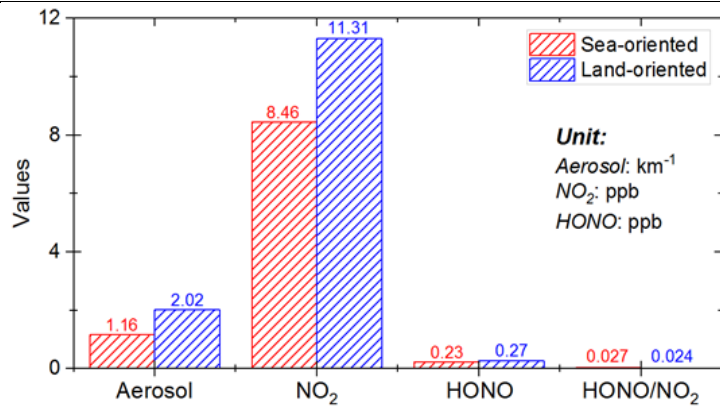
Figure 3. Bar plots of the averaged aerosol extinction, NO_2 concentration, HONO concentration, and $HONO/NO_2$ ratio during the campaign. The red and blue boxes denote sea-oriented and land-oriented measurements, respectively.
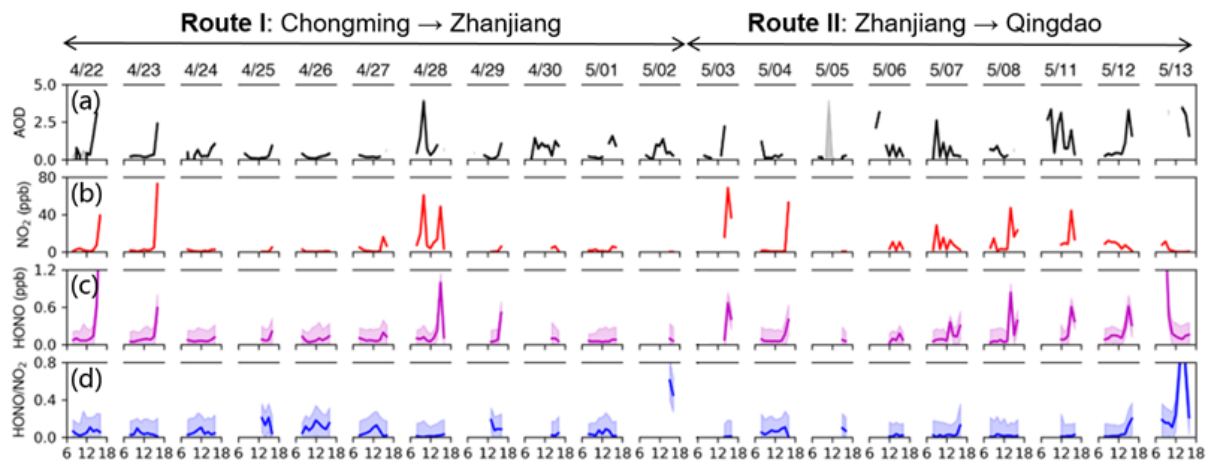
Figure 4. Histograms of the time series of (a) AOD, (b) surface NO_2 concentration, (c) surface HONO concentration, and (f) surface $HONO/NO_2$ ratios.
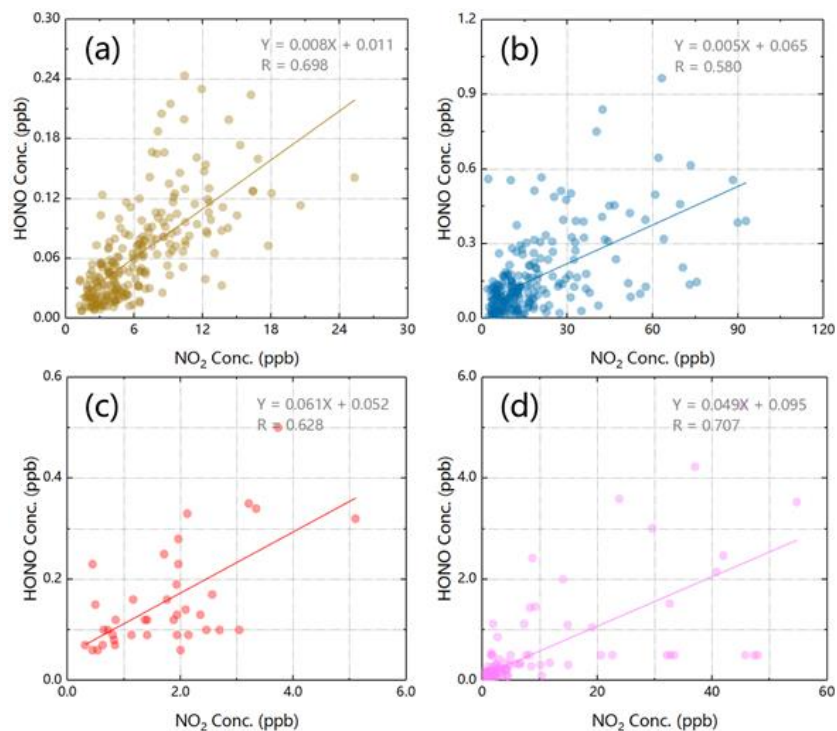
Figure 5. Linear regression plots between surface NO_2 and HONO concentrations in (a) CAMS, (b) SUST, and ship-based measurements of (c) sea-oriented and (d) land-oriented under static weather condition.

16

692
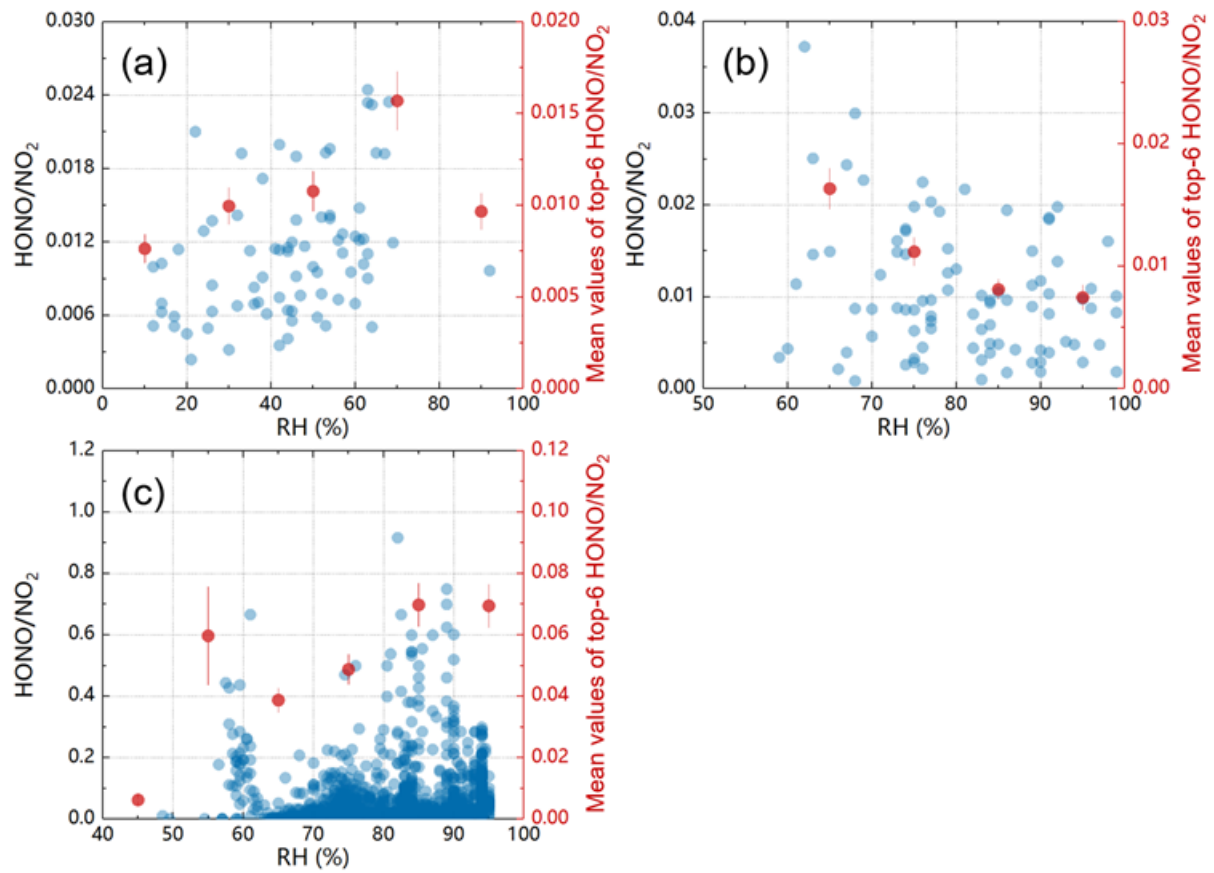
693
694   Figure 6. Scatter plots between RH and HONO/NO$_2$ ratios in (a) CAMS, (b) SUST, and (c) the ship-based campaign.

695
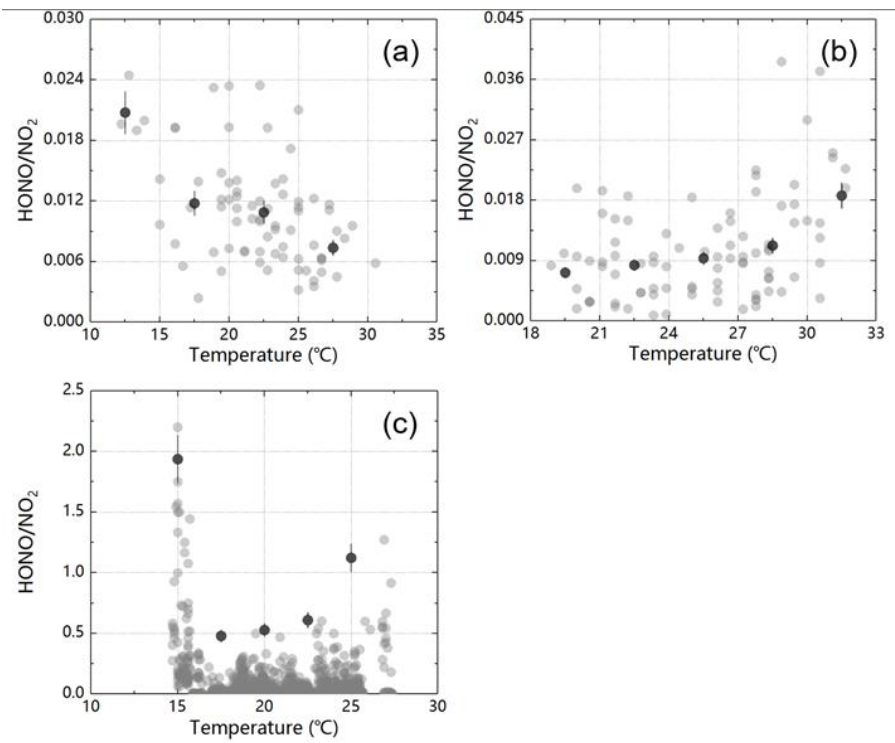
696
697   Figure 7. Scatter plots between temperature and HONO/NO$_2$ ratios in (a) CAMS, (b) SUST, and (c) the ship-based
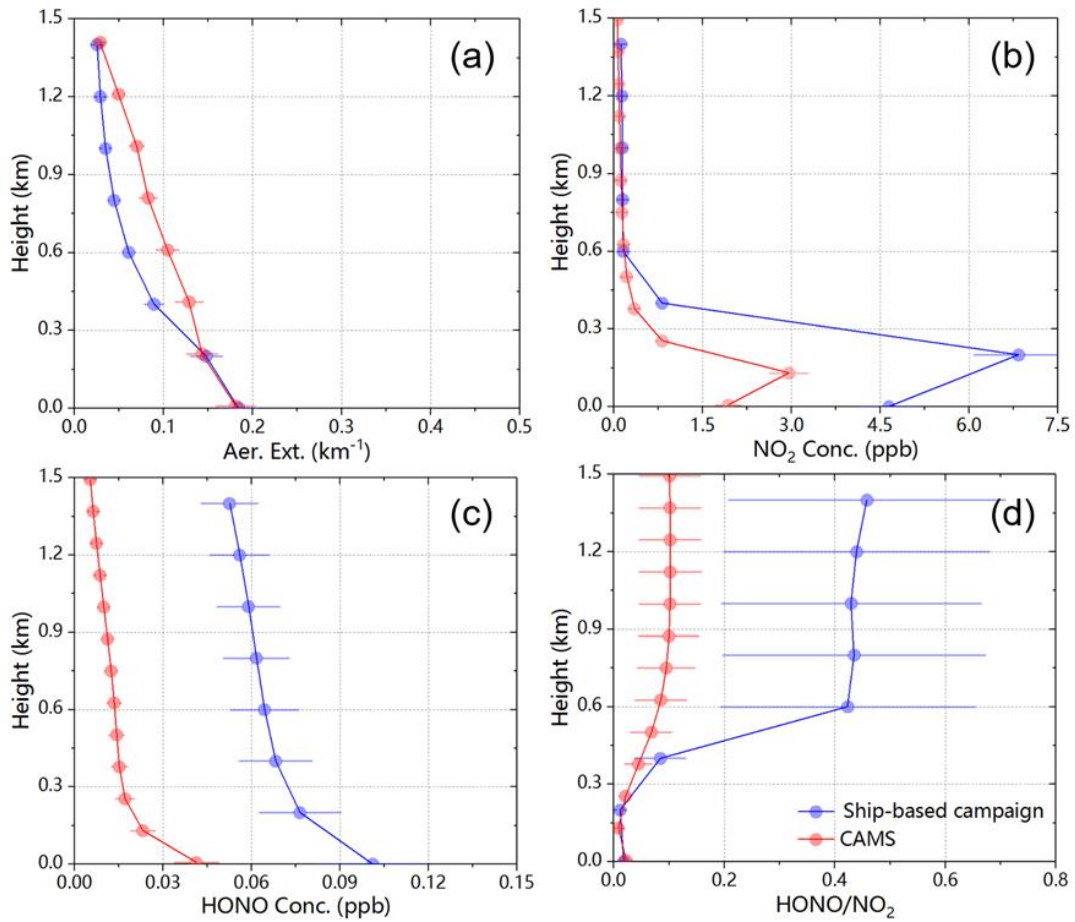698   campaign.

699

17
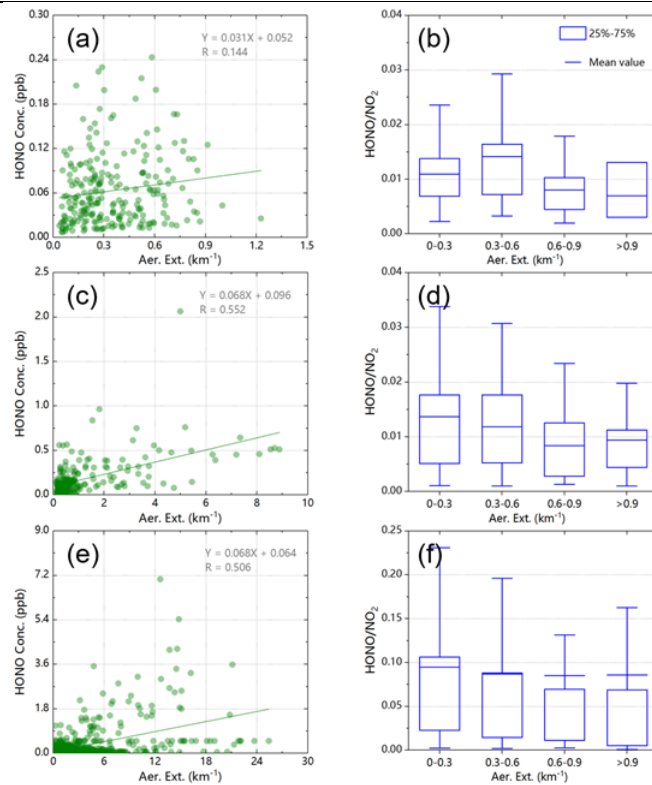
Figure 8. (a), (c), and (e) show the linear regression plots between surface aerosol extinction and HONO concentrations in CAMS, SUST and the ship-based campaign, respectively. Plots (b), (d), and (f) depicts the HONO/NO_2 ratio distribution under different aerosol extinction coefficient conditions in CAMS, SUST and the ship-based campaign.
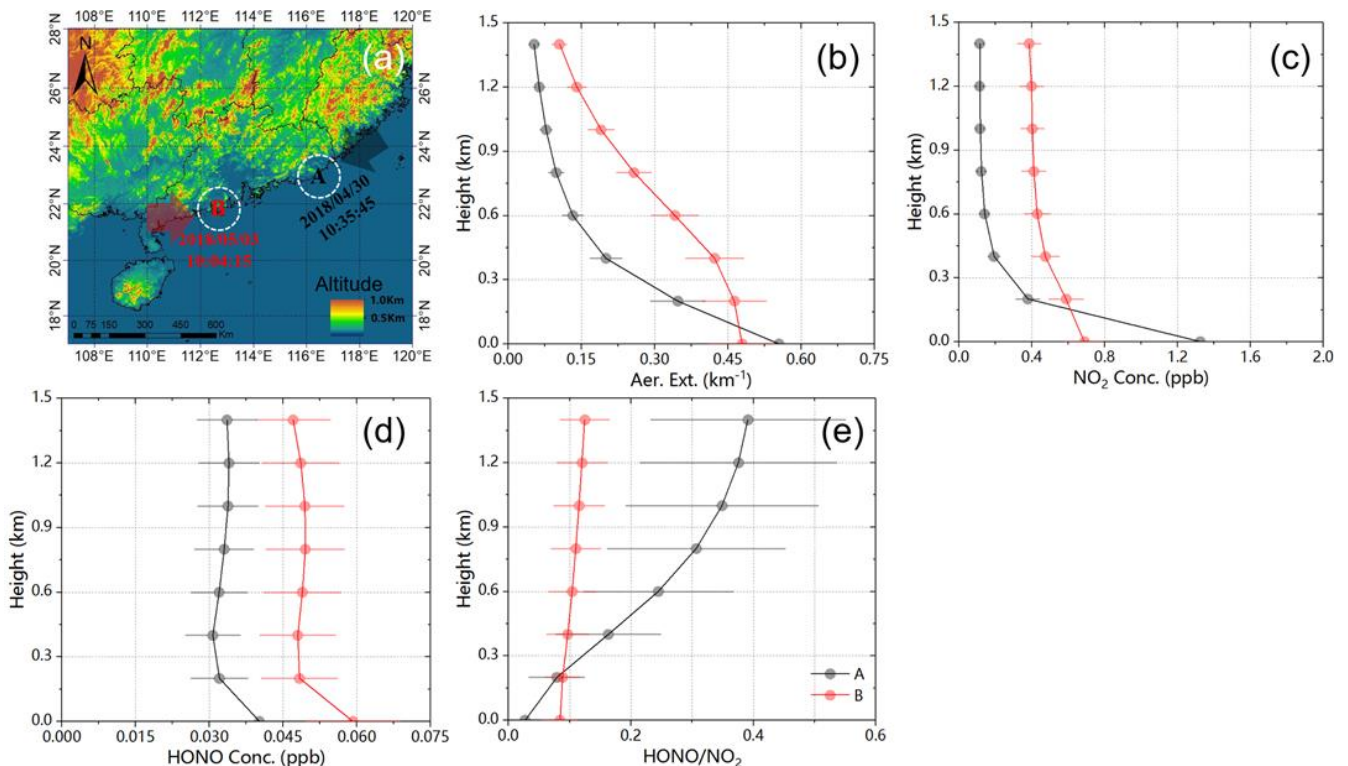
Figure 9. Map (a) shows the two measurement points (A: black, sea-oriented with sea wind; B: red, land-oriented with land wind) during the campaign. Plots (b)–(e) show the vertical profiles of aerosol, NO_2, HONO, and HONO/NO_2 ratios in the above two measurement points, respectively.

18

711
712 Figure 10. Plots showing the vertical distributions of (a) aerosol extinction, (b) NO_2 concentration, (c) HONO
713 concentration, and (d) HONO/NO_2 ratio. The blue and red lines represent a ship-based campaign case and a CAMS
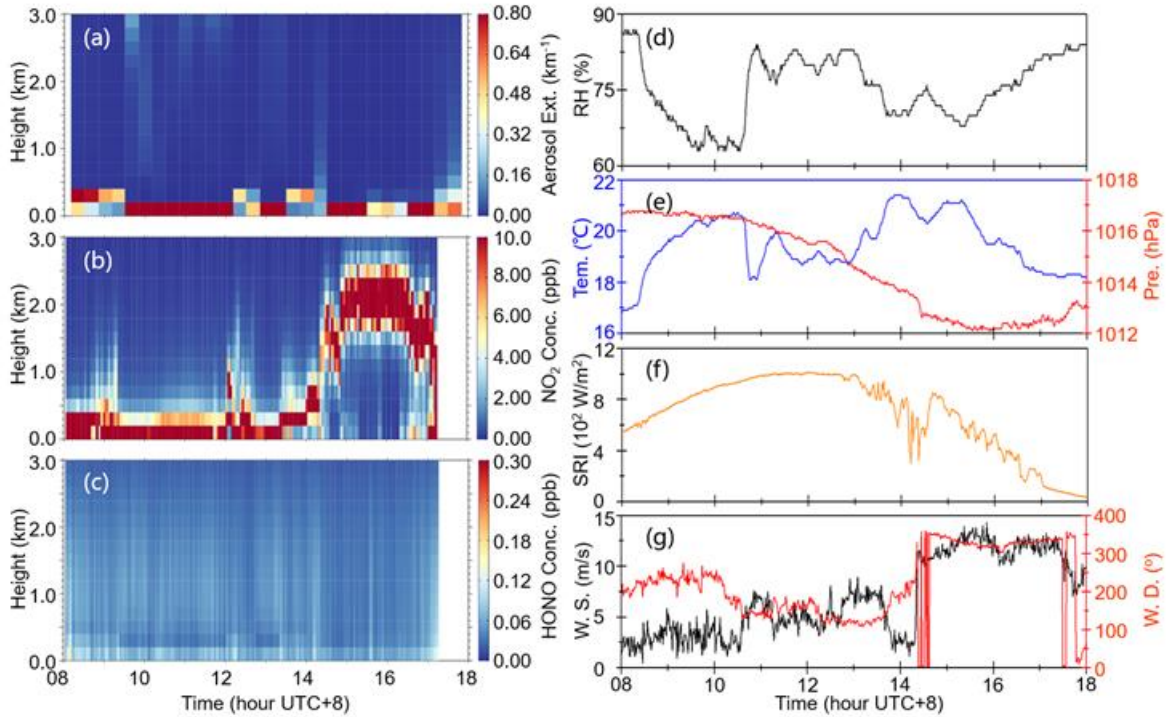714 case, respectively.

715

716

717
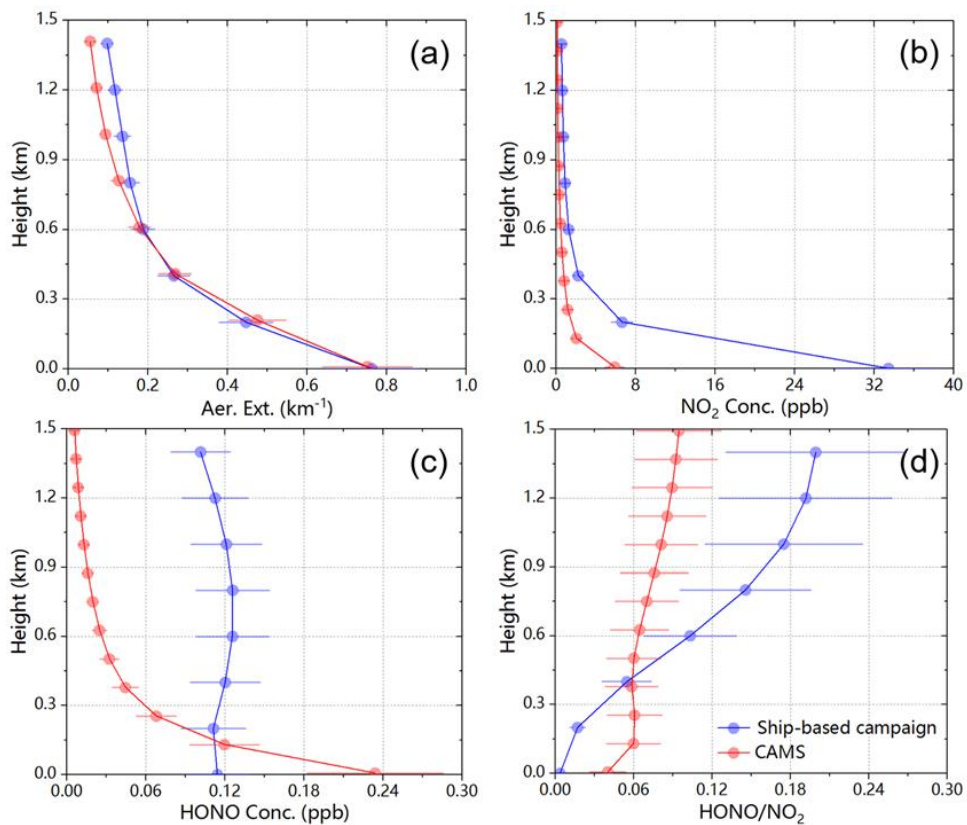
Figure 11. Plots showing the vertical distributions of (a) aerosol extinction, (b) NO$_2$ concentration, (c) HONO
concentration, and (d) HONO/NO$_2$ ratio. The blue and red lines represent a ship-based campaign case and a CAMS
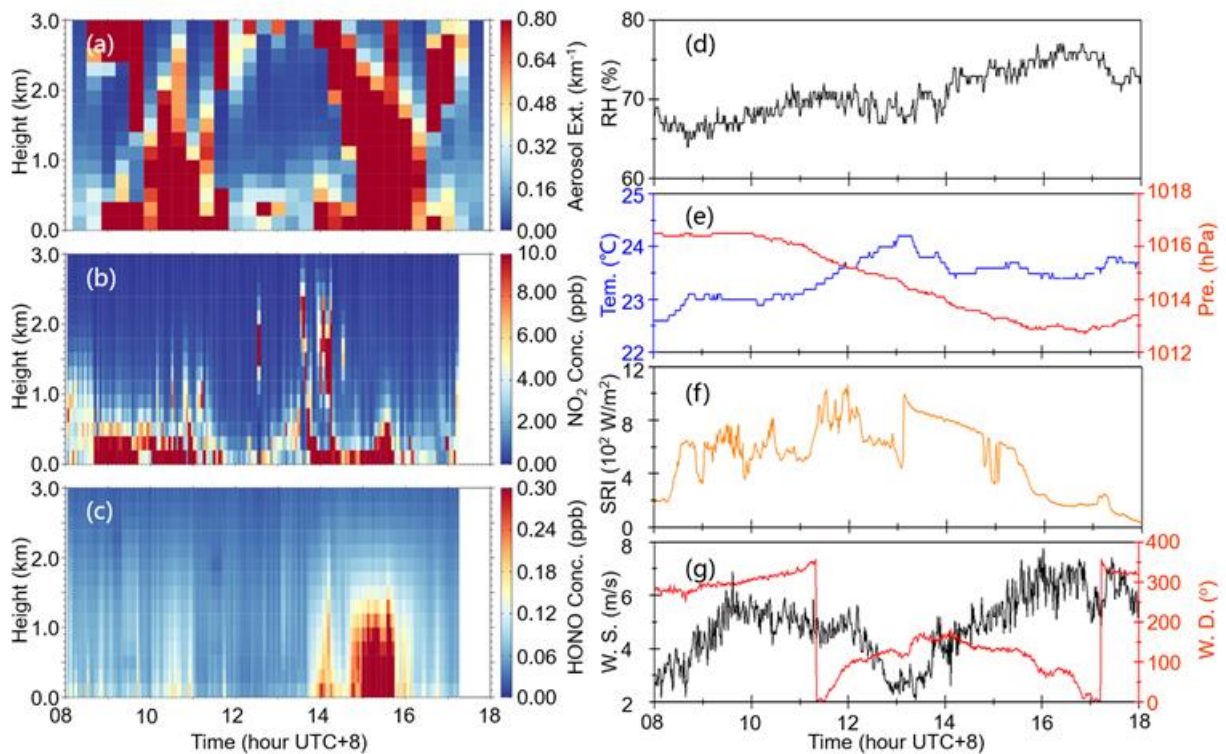case, respectively.

Figure 12. Case of 20 April 2018. Gradient image showing the time series of (a) aerosol extinction, (b) NO$_2$, and (c)
HONO vertical profiles. Plot (d) shows the time series of surface RH. Plot (e) depicts the time series of surface
temperature and pressure. Plot (f) shows the time series of surface SRI. (g) depicted the time series of surface wind
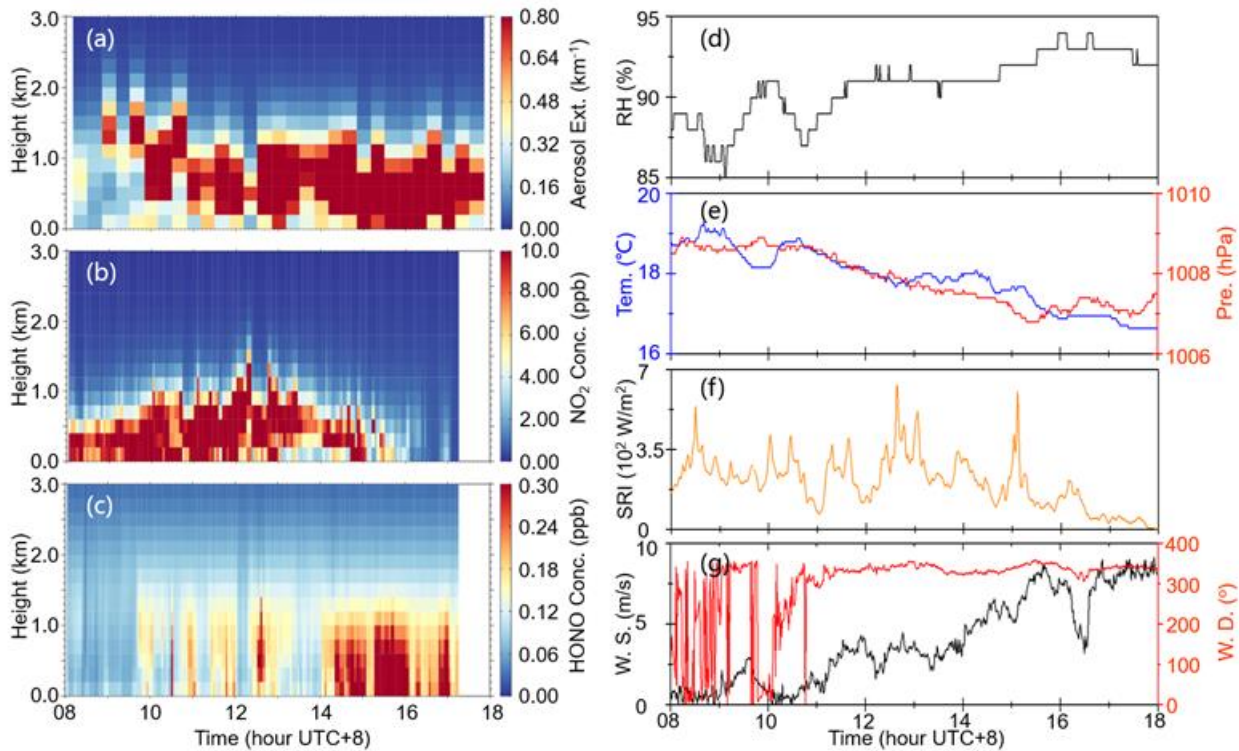speed and wind direction.

730 Figure 13. Case of 28 April 2018. Gradient image showing the time series of (a) aerosol extinction, (b) NO$_2$ and (c)
731 HONO vertical profiles, respectively. Plot (d) shows the time series of surface RH. Plot (e) depicts the time series of
732 surface temperature and pressure. Plot (f) shows the time series of surface SRI. Plot (g) depicts the time series of
733 surface wind speed and wind direction.

734

735
736 Figure 14. Case of 03 May 2018. Gradient image showing the time series of (a) aerosol extinction, (b) NO$_2$ and (c)
737 HONO vertical profiles, respectively. Plot (d) shows the time series of surface RH. Plot (e) depicts the time series of
738 surface temperature and pressure. Plot (f) shows the time series of surface SRI. Plot (g) depicts the time series of
739 surface wind speed and wind direction.